ETHANOL BASED SOL-GEL SYNTHESIS AND

CHARACTERIZATION OF HYDROXYAPATITE

A DISSERTATION REPORT

*Submitted in partial fulfillment of the
award of the degree
of*
MASTER OF TECHNOLOGY
in
NANOTECHNOLOGY

By

GOURI TREHAN

CENTRE OF NANOTECHNOLOGY
INDIAN INSTITUTE OF TECHNOLOGY ROORKEE
ROORKEE - 247 667 (INDIA)
JUNE, 2010

CANDIDATE'S DECLARATION

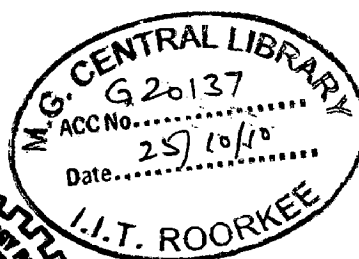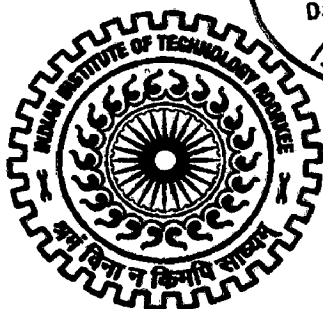*I hereby declare that the work which is being presented in this dissertation entitled "**ETHANOL BASED Sol-Gel SYNTHESIS AND CHARACTERIZATION OF HYDROXYAPATITE**" submitted in partial fulfillment of the requirement for the award of degree of **Master of Technology** in **NANOTECHNOLOGY**, submitted in the **Centre of Nanotechnology** at **Indian Institute of Technology Roorkee,** is an authentic record of my own work carried out under the guidance of **Dr. K. L. Yadav**, Associate Professor, Department of Physics, Indian Institute of Technology Roorkee, Roorkee.*

The matter embodied in this dissertation has not been submitted by me for the award of any other degree of this or any other Institute/University. In keeping with the general practice of reporting scientific observation, due acknowledgement has been made wherever the work described is based on the findings of other investigators.

Date:

Place: *Roorkee*

GOURI TREHAN

08551002

M.Tech. Nanotechnology

CERTIFICATE

This is to certify that the above declaration made by the candidate is correct to the best of my knowledge and belief.

Dr. K. L. Yadav,

ASSOCIATE PROFESSOR,

Department of Physics,

I.I.T. ROORKEE,

ROORKEE – 247667 (INDIA)

ACKNOWLEDGEMENT

I wish to express my deep sense of gratitude and sincere thanks to my guide **Dr. K. L. Yadav,** Associate Professor, Physics Department, Indian Institute of Technology, Roorkee, for his intuitive and meticulous guidance and perpetual inspiration in completion of this project work. Working under his guidance was a privilege and an excellent learning experience that I will cherish forever.

I would like to express my gratitude to **my parents**; their blessings, motivation and inspiration have always provided me a high mental support and contributed in all possible way, in completion of this project work.

I am also grateful to **my friends** who are actively involved in providing me vital support and encouragement whenever I needed.

Date: GOURI TREHAN

Place: Roorkee.   08551002

                                                                    M.Tech. Nanotechnology

                                                                    (II Year)

ABSTRACT

In this Dissertation report, a relatively easy method to synthesize pure, stable, stoichiometric nanocrystalline Hydroxyapatite i.e. $Ca_{10}(PO_4)_6(OH)_2$ (HAP) at low temperature by ethanol based sol–gel route, has been presented.

For the synthesis of Hydroxyapatite, equimolar solutions of $Ca(NO_3)_2.4H_2O$ and $(NH_4)_2HPO_4$ were dissolved in ethanol at 85 °C and the product so formed was sintered at three different temperatures, i.e. 400 °C, 750 °C and 1200 °C. These sintered samples along with the as prepared sample were then characterized by X-Ray Diffraction (XRD), Fourier Transform IR spectroscopy (FTIR), Scanning Electron Microscopy (SEM), Energy Dispersive X-ray spectroscopy (EDAX) and Thermogravimetric analysis (TGA)/Differential Thermal Analysis (DTA) for checking the formation and quality of desired product, for checking its stability at higher temperatures and for microstructural and compositional analysis.

TABLE OF CONTENTS

LIST OF FIGURES

canaliculi and lacunae [40]. Carbonated calcium-deficient hydroxyapatite is the main mineral of which dental enamel and dentin are comprised. Hydroxyapatite crystals are also found in the small calcifications (within the pineal gland and other structures) known as corpora arenacea or 'brain sand' [1, 2, 22].

Fig 1(a) Hydroxyapatite structure projected down the c-axis onto the basal plane. (Source: Posner, A. S., Perloff, A., and Diorio, A. D. 1958. Refinement of hydroxyapatite structure, Acta. Cryst. 11:308–309.)

HAP is commonly used as a filler to replace amputated bone or as a coating to promote bone ingrowth into prosthetic implants. Although many other phases exist with similar or even identical chemical makeup, the body responds much differently to them. Among the most important properties of hydroxyapatite as a biomaterial is its excellent biocompatibility. Hydroxyapatite appears to form a direct chemical bond with hard tissues [6-9]. On implantation of hydroxyapatite particles or porous blocks in bone, new lamellar cancellous bone forms within 4 to 8 weeks [48].

2

LIST OF FIGURES

CHAPTER 1

INTRODUCTION

Hydroxyapatite (HAP), also called Hydroxylapatite, is a naturally occurring mineral form of calcium apatite with the formula $Ca_5(PO_4)_3(OH)$, but is usually written $Ca_{10}(PO_4)_6(OH)_2$ to denote that the crystal unit cell comprises two entities. It is the hydroxyl endmember of the complex apatite group. The term "apatite" applies to a broad category of structures comprised of different constituents. Hydroxyapatite is one such constituent, another being carbonate (hydroxy) apatite, where carbonate ions may substitute for some of the hydroxyl ions (A-type) or the carbonate ions may be present on the phosphate sites (B-type) [23,24]. The OH^- ion can be replaced by fluoride, chloride or carbonate, producing fluorapatite, chlorapatite or carbonate (hydroxyl) apatite. HAP crystallizes into hexagonal rhombic prisms and has unit cell dimensions $a = 9.432Å$ and $c = 6.881Å$. The atomic structure of hydroxyapatite projected down the c-axis onto the basal plane is shown in Fig 1(i). Note that the hydroxyl ions lie on the corners of the projected basal plane and they occur at equidistant intervals (3.44 Å) along the columns perpendicular to the basal plane and parallel to the c-axis. Six of the ten calcium ions in the unit cell are associated with the hydroxyls in these columns, resulting in strong interactions among them [49]. The ideal Ca:P ratio of hydroxyapatite is 10:6 and the calculated density is 3.219 g/cm^3. It has a specific gravity of 3.08 and is 5 on the Mohs hardness scale. Pure hydroxyapatite powder is white. Naturally occurring apatites can, however, also have brown, yellow, or green colorations, comparable to the discolorations of dental fluorosis.

Approximately 70% (by weight) of natural bone is made up of the inorganic mineral hydroxyapatite (known as bone mineral). Living bone constantly undergoes a coupled resorptive-formative process known as bone remodeling. The process involves simultaneous bone removal and replacement through the respective activities of osteoblasts and osteoclasts, with the accompanying vascular supply and a network of

canaliculi and lacunae [40]. Carbonated calcium-deficient hydroxyapatite is the main mineral of which dental enamel and dentin are comprised. Hydroxyapatite crystals are also found in the small calcifications (within the pineal gland and other structures) known as corpora arenacea or 'brain sand' [1, 2, 22].
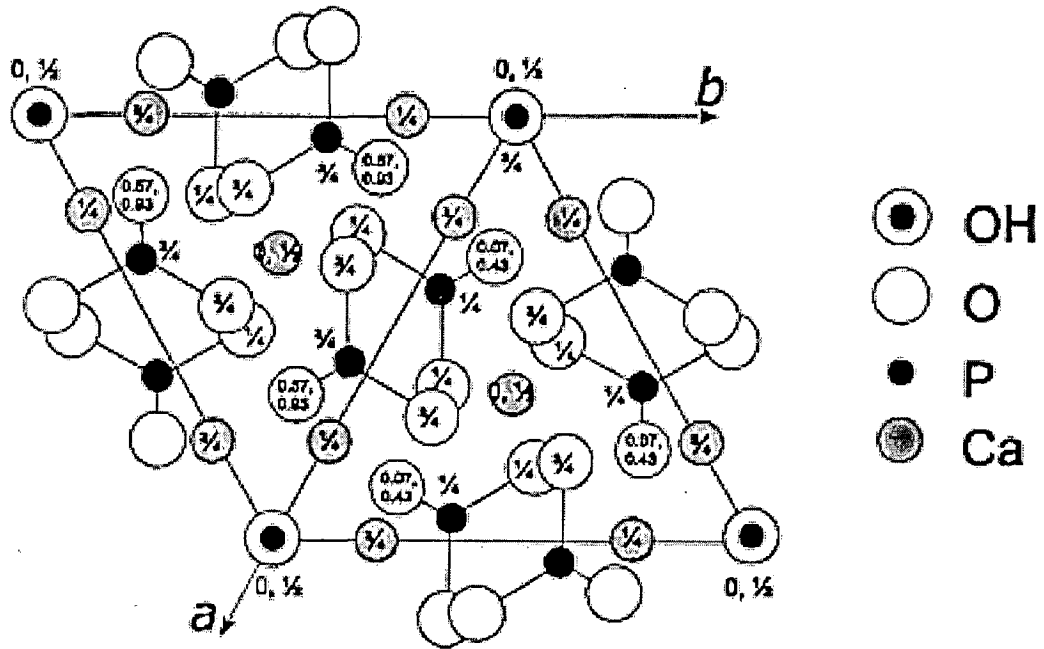

Fig 1(a) Hydroxyapatite structure projected down the c-axis onto the basal plane. (Source: Posner, A. S., Perloff, A., and Diorio, A. D. 1958. Refinement of hydroxyapatite structure, Acta. Cryst. 11:308–309.)

HAP is commonly used as a filler to replace amputated bone or as a coating to promote bone ingrowth into prosthetic implants. Although many other phases exist with similar or even identical chemical makeup, the body responds much differently to them. Among the most important properties of hydroxyapatite as a biomaterial is its excellent biocompatibility. Hydroxyapatite appears to form a direct chemical bond with hard tissues [6-9]. On implantation of hydroxyapatite particles or porous blocks in bone, new lamellar cancellous bone forms within 4 to 8 weeks [48].

2

Synthetic hydroxyapatite has long been recognized as one of the most important bone substitute materials in orthopaedics and dentistry over past few decades because of its chemical and biological similarity to the mineral phase of human bone [3-5, 20, 22]. However, most synthetic apatites are formed via high temperature processes (e.g. sintering), resulting in a well-crystallized structure, which has little or no activity towards bioresorption. This is in contrast to nanocrystalline or bio-crystal apatites, which are typically non-stoichiometric, and which typically exhibit much higher degree of bioactivity. Recently, the use of sol–gel processes for synthesis of hydroxyapatite (HAP) became an important research objective [10-16]. Low temperature formation and fusion of the apatitic crystals has been the main contributions of the sol–gel process, in comparison to conventional methods [37-39]. For instance, temperatures higher than $1000°$ C are usually required to sinter the fine apatite crystals prepared from wet precipitation, whilst several hundred degree Celsius lower than above are needed to densify sol–gel HAP [17-18]. Moreover, processing of sol–gel HAP usually results in a fine-grain microstructure containing a mixture of nano-to-submicron crystals, better accepted by the host tissue. A recent study indicated that a specific aging time period either at ambient or higher temperature is necessary to form a phase-pure apatite [19]. Insufficient aging causes appearance of impurity phases, such as CaO or $CaCO_3$.

A major concern in the synthesis of Hydroxyapatite is to maintain the pH level greater than 9, as a reduction in the pH leads to the formation of calcium-deficient apatite structures. Furthermore, the formation of hydroxyapatite is not complete until the final stages of sintering, and often sintering at elevated temperatures leads to the decomposition of hydroxyapatite leading to the formation of tricalcium phosphate.

The sol–gel derived apatite films or coatings show to have a tailored chemical composition, crystallinity, microstructure and a good adhesion strength. Sol–gel technique shows a great promising potential for preparing bioactive materials. For medical applications, bioactive apatite films are of great importance because the bioactive film coated titanium alloy implants can combine the mechanical advantages of the metal with biological affinity of apatite to natural tissue; as a result, healing time can be

3

shortened [25]. However, an apatite film functioned as a bioactive film on metallic implants should have a reasonably good stability to withstand dissolution of the film while in contact with the body fluid [26], rough or porous surface morphology to increase joint area with natural bone [27], and good adhesion strength to maintain a strong bridge to connect the implant with bone tissue [28]. Hence, it is a prior task to make the films meet the requirements for any film preparation method. Sol–gel technique is versatile and capable of controlling preparation process, eventually high quality bioactive films are able to be obtained.

The aim of the present work was to synthesize nanocrystalline hydroxyapatite powders using a sol-gel route with simple procedures and relatively inexpensive chemicals. This would enable an understanding of the means available to overcome the limitations of the extremely slow rate of hydrolysis of phosphate esters. The influence of slight variations in the stoichiometry of the precursors on the final formed phase was also studied.

CHAPTER 2

LITERATURE REVIEW

1. T. Anee Kuriakose et al. presented a relatively easy method to synthesize pure, stable, stoichiometric nano crystalline hydroxyapatite, $Ca_{10}(PO_4)_6(OH)_2$, HAP at low temperature by sol–gel route using equimolar solutions of $Ca(NO_3)_2.4H2O$ and $(NH_4)_2HPO_4$ dissolved in ethanol at 85°C. Then the product was sintered at 400°C, 750°C and 1200°C and then characterized by chemical analysis, XRD, FT-IR, SEM and TGA/DTG. The synthesized HAP was found to be stable upto 1200°C without any by-products.

2. Berry EE et al. presented that when amorphous calcium phosphate (ACP) was transformed to crystalline hydroxyapatite (HAP) in a series of aqueous slurry concentrations ranging from low to high, the higher slurry concentrations produced more Ca-deficient HAP as measured by Ca/P ratio and heat-produced pyrophosphate. The excess solution phosphate produced in the higher slurry transformations results in lower Ca/P ratio HAP. It was suggested that an ACP is the precursor to bone apatite. Regulation of the in vivo ACP slurry concentration could then control the stoichiometry and, therefore, the metabolic activity of bone apatite.

3. Dean-Mo Liu et al. investigated structural evolution upon transformation of sol to gel, and gel to final ceramic during the synthesis of hydroxyapatite using Fourier transform infrared (FTIR) analysis, X-ray diffraction (XRD), thermal behavior (DTA and TGA), and electron microscopy examination (SEM/TEM). They first aged sol thermally at 45°C for various time periods up to 120 min. The colloidal sol, which may have an oligomeric structure, was found relatively stable against coagulation. Upon drying, the sol particles consolidated into dry gel through van der Waals attraction, and showed X-ray amorphous phosphate structure. The solid

5

gels showed a particulate microstructure, composed of primary particles of about 8–10nm in diameter. The amorphous gel transformed into crystalline apatite at temperatures >300°C. The calcined gels showed a nano-scale microstructure, with grains of 20–50nm in diameter. Through an appropriate heat treatment between 300 °C and 400 °C, the apatite prepared using current process exhibits a nano-scale, low-crystallinity, carbonated apatitic structure, which closely resembles that of human bone apatite.

4. A. Jillavenkatesa et al. synthesized Hydroxyapatite using the sol gel processing route. The formation of hydroxyapatite and other compounds during the heat-treatment cycle were identified and characterized using thermal analyses and X-ray diffraction together with infrared and Raman spectroscopy. The influence of the addition of various organic alcohols (R-OH, R=CH_3-, C_2H_5- and C_3H_8-) on the reaction results was studied.

5. Wenjian Weng and Sam Zhang showed in their work that the surface of biomedical metallic implants covered by a bioactive apatite film can create bioactivity of the implant and shorten healing time. They prepared apatite films on Ti_6Al_4V by sol–gel route using $Ca(NO_3)_2$, P_2O_5 and HPF_6 as the precursors, in vitro evaluations of the resulting hydroxyapatite (HAP) and fluorapatite hydroxyapatite solid solution (FHA) films were done in Kokubo's simulated body fluid and citric acid modified phosphate buffer solution (CPBS). HPF_6 showed a good reagent for the incorporation of fluorine into apatite films. The FHA film demonstrated to have good bioactivity, and to have better stability in CPBS and higher adhesion strength than the HAP film. When fluorine was incorporated into the film, then an increase in crystallinity of the apatite film and a decrease in intrinsic solubility of the FHA film could make significant contributions to the improvement in the stability; the thermal expansion coefficient of the FHA film getting closer to that of Ti_6Al_4V could be responsible for the increase in adhesion strength.

6. C.M. Lopatin and V. Pizziconi studied the formation of hydroxyapatite (HA) from a sol-gel precursor using X-ray diffraction (XRD). The sol-gel was processed into both powders and thin films. The effect of drying and firing temperatures on the HAP phase formation was studied. Thin HAP films up to 1 μm thick were deposited on silicon wafers coated either with borophosphate silicate glass (BPSG) or titanium films, dried and then fired. Increasing the drying temperature raised the firing temperature for initial formation of crystalline HAP. It was found that at firing temperatures ranging from 300°C to 1000°C, the dominant phase in the powders was HAP with small amounts of calcium oxide and β-tricalcium phosphate (β-TCP). As the firing temperature increased the amount of CaO and β-TCP increased. At firing temperatures ranging from 300 °C to 500°C the only observable crystalline phase in the films was HAP.

7. Liu DM et al. synthesized Hydroxyapatite (HAP) ceramics using a sol gel route with triethyl phosphite and calcium nitrate as phosphorus and calcium precursors, respectively. Two solvents, water and anhydrous ethanol, were used as diluting media for HAP sol preparation. The sols were stable and no gelling occurred in ambient environment for over 5 days. The sols became a white gel only after removal of the solvents at 60 °C. X-ray diffraction showed that apatitic structure first appeared at a temperature as low as 350 °C. The crystal size and the HAP content in both gels increase with increasing calcination temperature. The type of initial diluting media (i.e., water vs. anhydrous ethanol) did not affect the microstructural evolution and crystallinity of the resulting HAP ceramic. The ethanol-based sol dip-coated onto a Ti substrate, followed by calcination at 450°C, was found to be porous with pore size ranging from 0.3 to 1 μm. This morphology is beneficial to the circulation of physiological fluid when the coating is used for biomedical applications. The satisfactory adhesion between the coating and substrate suggests its suitability for load-bearing uses.

8. A.Cuneyt Tas prepared Hydroxyapatite (HAP, $Ca_{10}(PO_4)_6(OH)_2$), as a nano-sized (~50 nm), homogeneous and high-purity ceramic powder from calcium nitrate tetrahydrate and diammonium hydrogen phosphate salts dissolved in modified synthetic body fluid (SBF) solutions at 37 °C and pH of 7.4 using a novel chemical precipitation technique. The synthesized precursors were found to easily reach a phase purity 99 % after 6 h of calcination in air atmosphere at 900 °C, following oven drying at 80 °C. There was observed, surprisingly, no decomposition of HAP into the undesired b-TCP phase even after heating at 1600 °C in air for 6 h. This observation showed the superior high-temperature stability of such & biomimetic HAP powders as compared to those reported in previous studies. The former powders were also found to contain trace amounts of Na and Mg ions, originating from the use of SBF solutions instead of pure water during their synthesis. Characterization and chemical analysis of the synthesized powders were performed by X-ray powder diffraction, energy-dispersive X-ray spectroscopy, Fourier transform infra-red spectroscopy, scanning electron microscopy, and inductively coupled plasma atomic emission spectroscopy.

9. M.P. FERRAZ et al. presented a review of preparation methodologies for HAP. Hydroxyapatite (HAP) has been widely used as a biocompatible ceramic in many areas of medicine, but mainly for contact with bone tissue, due to its resemblance to mineral bone. In mammals, the skeleton presents a carbonated and partially substituted apatite, based on nanocrystal aggregates, and associated with collagen, building up 3-D structures present in various bone tissue conformations like trabecular or cancellous bone. There has been growing interest in developing bioactive synthetic ceramics that could closely mimic natural apatite characteristics. This review presents some of the most well known forms of obtaining, by precipitation methods, nanophased HA. Some traditional and more recent developments vis-à-vis the possible HA nanoparticles applications are discussed.

10. I. Rehman and W. Bonfield studied the structure of different commercial synthetic hydroxyapatite powders and a novel carbonated apatite with photo-acoustic (PAS) Fourier transform infrared (FTIR) spectroscopy. The PAS technique is an ideal method for analysing biomaterials, as materials can be analyzed without the need to reduce the particle size or to dilute with KBr Spectra from carbonated apatite appear to be different from those of commercial hydroxyapatite powders, with the main difference lying in the carbonate and phosphate ratio. Commercial hydroxyapatite powders from different sources have also been analyzed and compared.

CHAPTER 3

MATERIALS AND METHODS

3.1. REAGENTS USED:

(a) $Ca(NO_3)_2.4H_2O$ (Merck)

(b) $(NH_4)_3PO_4$ (Merck)

(c) $Ca(OH)_2$

(d) Ethanol

3.2. INSTRUMENTS AND EQUIPMENTS USED:

(a) Nicolet 60 SX FTIR spectrometer (**Nicolet Instruments Corporation, Madison, WI**).

(b) X-ray powder diffractometer (**Brucker D8 Advance**).

(c) The Thermo gravimetric analysis (TGA) coupled with differential thermal analysis (DTA) (**METTLER TA 4000 System**).

(d) Energy dispersive X-ray spectrometer (EDX) attached to the field emission scanning electron microscope (FESEM) (**FEI, Quanta 200i**).

(e) Magnetic Stirrer (**REMI**).

(f) Tube Furnace.

3.3. CHARACTERIZATION TECHNIQUES USED:

3.3.1. X-Ray Diffraction (XRD):

X-ray powder diffraction (XRD) is a rapid analytical, non-destructive technique primarily used for phase identification of a crystalline material and can provide information on unit cell dimensions, chemical composition, and physical properties of materials. This technique is based on observing the scattered intensity of an X-ray beam hitting a sample as a function of incident and scattered

10

angle, polarization, and wavelength or energy. Computer analysis of the peak positions and intensities associated with this pattern enables qualitative analysis, lattice constant determination and/or stress determination of the sample. Qualitative analysis may be conducted on the basis of peak height or peak area. The peak angles and profiles may be used to determine particle diameters and degree of crystallization, and are useful in conducting precise X-ray structural analysis. The identification of single or multiple phases in an unknown sample is the main application of X-ray powder diffractometry.

When a monochromatic X-ray beam with wavelength *lambda* is projected onto a crystalline material at an angle *theta*, diffraction occurs only when the distance travelled by the rays reflected from successive planes differs by a complete number *n* of wavelengths.

Bragg's Law

By varying the angle *theta*, the Bragg's Law conditions are satisfied by different *d*-spacings in polycrystalline materials. Plotting the angular positions and intensities of the resultant diffracted peaks of radiation produces a pattern, which is characteristic of the sample. Where a mixture of different phases is present, the resultant diffractogram is formed by addition of the individual patterns. The diffraction data is compared against a database maintained by International Centre for Diffraction Data.

X-ray diffractometers consist of three basic elements: an X-ray tube, a sample holder, and an X-ray detector. X-rays are generated in a cathode ray tube by heating a filament to produce electrons, accelerating the electrons toward a target by applying a voltage, and bombarding the target material with electrons. When electrons have sufficient energy to dislodge inner shell electrons of the target material, characteristic X-ray spectra are produced. These spectra consist of several components, the most common being K_α and K_β. K_α consists, in part, of $K_{\alpha 1}$ and $K_{\alpha 2}$.

Copper is the most common target material for single-crystal diffraction, with Cu K_α radiation = 0.5418Å. These X-rays are collimated and directed onto the

sample. As the sample and detector are rotated, the intensity of the reflected X-rays is recorded. When the geometry of the incident X-rays impinging the sample satisfies the Bragg Equation, constructive interference occurs and a peak in intensity occurs. A detector records and processes this X-ray signal and converts the signal to a count rate which is then output to a device such as a printer or computer monitor.
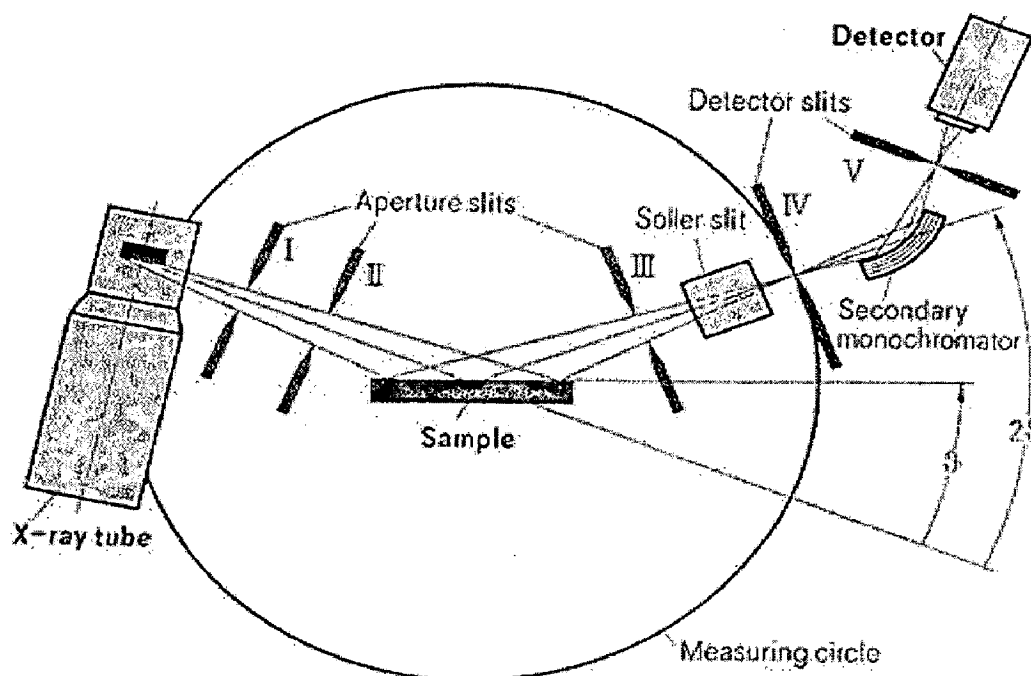

Fig 3 (a) Configuration of a XRD unit

The geometry of an X-ray diffractometer is such that the sample rotates in the path of the collimated X-ray beam at an angle θ while the X-ray detector is mounted on an arm to collect the diffracted X-rays and rotates at an angle of 2θ. The instrument used to maintain the angle and rotate the sample is termed a *goniometer*.
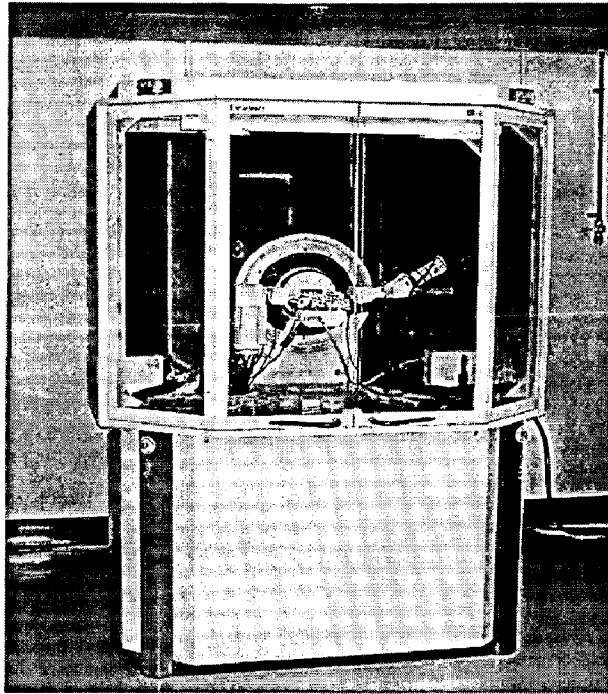
Fig 3 (b) X-ray powder diffractometer (Brueker D8 Advance)

3.3.2. FESEM:

FESEM stands for Field emission scanning electron microscope. The FESEM is a microscope that uses electrons instead of light to form an image. Since their development in the early 1950's, scanning electron microscopes have developed new areas of study in the medical and physical science communities. The FESEM has allowed researchers to examine a much bigger variety of specimens.

The scanning electron microscope has many advantages over traditional microscopes. The FESEM has a large depth of field, which allows more of a specimen to be in focus at one time. The FESEM also has much higher resolution, so closely spaced specimens can be magnified at much higher levels. Because the FESEM uses electromagnets rather than lenses, the researcher has much more control in the degree of magnification. All of these advantages, as well as the actual strikingly clear images, make the scanning electron microscope one of the most useful instruments in research today.

13

Various parts of FESEM:

The sample is fixed with conductive tape (10) on a metallic sample block (11) (see close-up picture of such block with test samples here below). Non-conductive specimen is coated with a nanometer thin-layer of metal to facilitate emission and flow of electron in the surface. The metal block is crewed on a sample holder (9) and positioned in the pre-vacuum chamber (7), an intermediate chamber with a front and a rear lid. This chamber acts as a lock. When the vacuum in this space is low enough the shutter to the high vacuum (lowest pressure) is opened and the object is shifted with a long rod (8) into the object chamber on a rail just under the column (1). In order to ease the positioning a one can observe the inner view of the object chamber with an infra red camera. The object chamber is the place where the sample is irradiated by the electron beam. The position of the sample stage can be adjusted in height (z-navigation 5) and horizontally (x-y navigation; 6). The topographical scanning electron imaging requires a secondary electrons detector (4), like in a normal SEM there is a control panel (13), a monitor for the operation of the device (15) and one showing the SE images (14). A separate EDS detector (3) allows one to capture the X-ray scanning and there is another back-scattered electron detector. In this chamber in the heart of the electron microscope the vacuum is extremely low: 10^{-6}mBar (thus 1:1.000.000.000 the normal atmospheric pressure!; vacuum display = 16; around the electron gun the vacuum is even two orders of magnitude lower!). The need for such extreme vacuum is that collision of bombarding electrons from the beam with gas molecules in the column would result in heat production. Cooling (18) and supply of electric power (19) are required in order to maintain this extreme vacuum.

Under vacuum, electrons generated by a Field Emission Source are accelerated in a field gradient. The beam passes through Electromagnetic Lenses, focussing onto the specimen. As result of this bombardment different types of electrons are emitted from the specimen. A detector catches the secondary electrons and an image of the sample surface is constructed by comparing the intensity of these

secondary electrons to the scanning primary electron beam. Finally the image is displayed on a monitor.

Electron Emission
Cathode

Anodes

Cathode ray tube (synchronized with scanning coil)

Scanning unit

CRT

Electro magnetic lenses

Secondary electrons

Specimen stage

Digital processing signal

Electron detector
(scintillator)
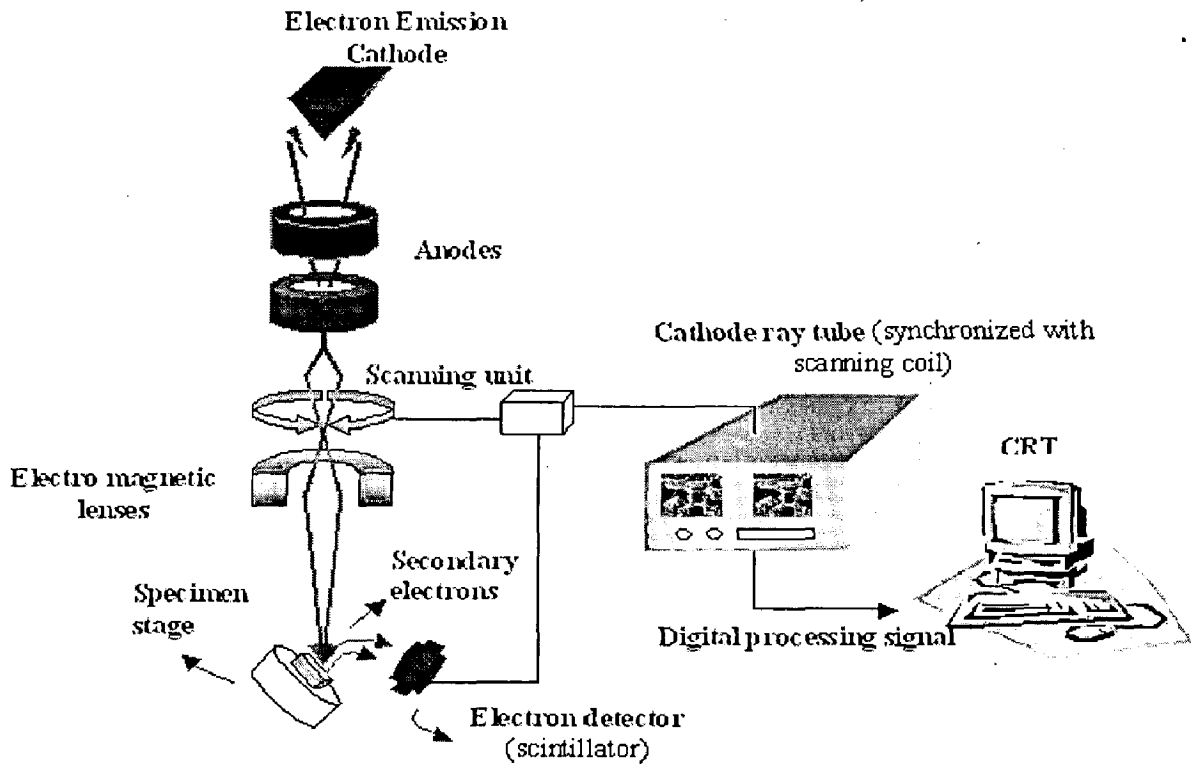
Fig 3 (c) FESEM working principle

In SEM the image is formed from **secondary electrons** that have been dislocated at the surface of the scanned sample by bombarding primary electrons from the electron gun. Those ejected electrons are captured by a detector and the information is converted into an electric signal, amplified and digitalized. The result is a topographical image of the *surface* of the object, e.g. the surface of a metal coating or lamellae of fish gills (see example here below). Besides secondary electrons, radiation (in particular X-rays and cathodoluminescence in typical samples) as well as back-scattered and so-called Auger electrons with an own energy level are produced upon interaction of atoms in the surface layer of the sample with the primary electron beam. These emission signals, which contain

15

information among others on the element composition of the upper layer, can be received by selected detectors, as is the case in EDAX microscopes for example, and combined with the topographical image.

Besides, there are scanning electron microscopes which are equipped with **EDS** (Energy Dispersed Spectroscopy) or EDAX (Energy-Dispersed Analysis of X-rays) detectors that capture the emitted X-ray. With such instruments it is possible to determine which elements are present in the surface layer of the sample (at a depth in the micrometer range) and where these elements are present ("mapping technique"). This particular microscope also allows one to capture directly reflected electrons, the so-called **back scattered electrons**, from which one can obtain a global appreciation whether one or several elements are present in the surface layer of the sample. Also the so-called Auger electrons, which are emitted just under the surface, provide information about the nature of the atoms in the sample.

SAMPLE PREPARATION FOR FESEM:

Because the SEM utilizes vacuum conditions and uses electrons to form an image, special preparations must be done to the sample. All water must be removed from the samples because the water would vaporize in the vacuum. All metals are conductive and require no preparation before being used. All non-metals need to be made conductive by covering the sample with a thin layer of conductive material. This is done by using a device called a "sputter coater."

The sputter coater uses an electric field and argon gas. The sample is placed in a small chamber that is at a vacuum. Argon gas and an electric field cause an electron to be removed from the argon, making the atoms positively charged. The argon ions then become attracted to a negatively charged gold foil. The argon ions knock gold atoms from the surface of the gold foil. These gold atoms fall and settle onto the surface of the sample producing a thin gold coating.

The bombarding electrons (= **primary electrons**) can penetrate in the electron shells of the atoms composing the surface of the sample. The energy (negative charge, mass, velocity) of these incident electrons can be converted to eject local electrons, so-called **secondary electrons**, from the shells of the atoms in the surface of the specimen. This information cab ne utilized to reconstruct a detailed topographical image of the sample (SEI = Secondary Electrons Imaging). The final image looks like a shadow-cast photograph of the surface of the sample. This record of the morphology is the best-known application of a scanning electron microscope.

Primary electron can also be reflected by atoms at about 10-100 nanometre depth at the surface. These so-called "**back-scatter**" conserve their energy at incidence, but their direction of propagation has been modified upon interaction. One can obtain a rough representation whether the surface of the sample is constituted of a single or multiple elements. At the surface of the sample electrons in the deeper electron shells can be ejected by primary electrons, resulting in an electron hole. When this lower-shell position is filled by an electron from higher shell energy is released. This can be as light (photons; the phenomenon is also called cathode luminescence) or as **X-ray**. Because each element emits an own characteristic energy value, the elements present in the micrometer range depth of the sample can be determined. See example here below. Another phenomenon is that the energy released upon filling a hole in the K shell by an electron from the L shell is used to expulse an electron from the external M shell: a so-called **Auger electron**. The released energy is characteristic for the type of atom. Auger electrons are produced in the outermost surface layer (at nanometer depth) of the sample.

3.3.3. EDAX:

Energy dispersive X-ray spectroscopy (EDS) is an analytical technique used for the elemental analysis or chemical characterization of a sample. It is one of the variants of XRF. As a type of spectroscopy, it relies on the investigation of a sample through interactions between electromagnetic radiation and matter,

analyzing x-rays emitted by the matter in response to being hit with charged particles. Its characterization capabilities are due in large part to the fundamental principle that each element has a unique atomic structure allowing x-rays that are characteristic of an element's atomic structure to be identified uniquely from each other.

To stimulate the emission of characteristic X-rays from a specimen, a high energy beam of charged particles such as electrons or protons , or a beam of X-rays, is focused into the sample being studied. At rest, an atom within the sample contains ground state (or unexcited) electrons in discrete energy levels or electron shells bound to the nucleus. The incident beam may excite an electron in an inner shell, ejecting it from the shell while creating an electron hole where the electron was. An electron from an outer, higher-energy shell then fills the hole, and the difference in energy between the higher-energy shell and the lower energy shell may be released in the form of an X-ray. The number and energy of the X-rays emitted from a specimen can be measured by an energy dispersive spectrometer. As the energy of the X-rays are characteristic of the difference in energy between the two shells, and of the atomic structure of the element from which they were emitted, this allows the elemental composition of the specimen to be measured.
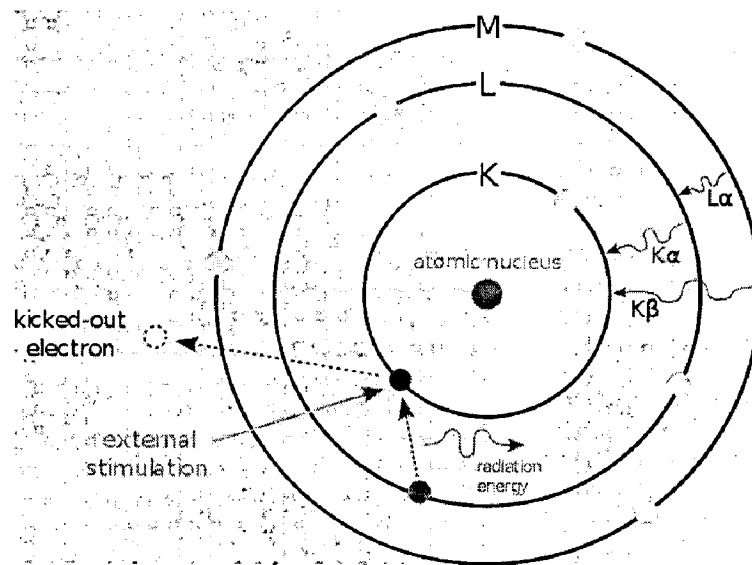

Fig 3 (d) Principle of EDAX

3.3.4. Fourier Transform Infrared (FTIR) Spectroscopy:

Fourier transform infrared (FTIR) spectroscopy is a measurement technique that allows one to record infrared spectra. It is most useful for identifying chemicals that are either organic or inorganic. It can be utilized to quantitate some components of an unknown mixture. It can be applied to the analysis of solids, liquids, and gasses. The term Fourier Transform Infrared Spectroscopy (FTIR) refers to a fairly recent development in the manner in which the data is collected and converted from an interference pattern to a spectrum. Unlike a dispersive instrument, i.e. grating monochromator or spectrograph, the FT-IR Spectrometer collects all wavelengths simultaneously. This feature is called the Multiplex or Felgett Advantage.

Today's FTIR instruments are computerized which makes them faster and more sensitive than the older dispersive instruments.
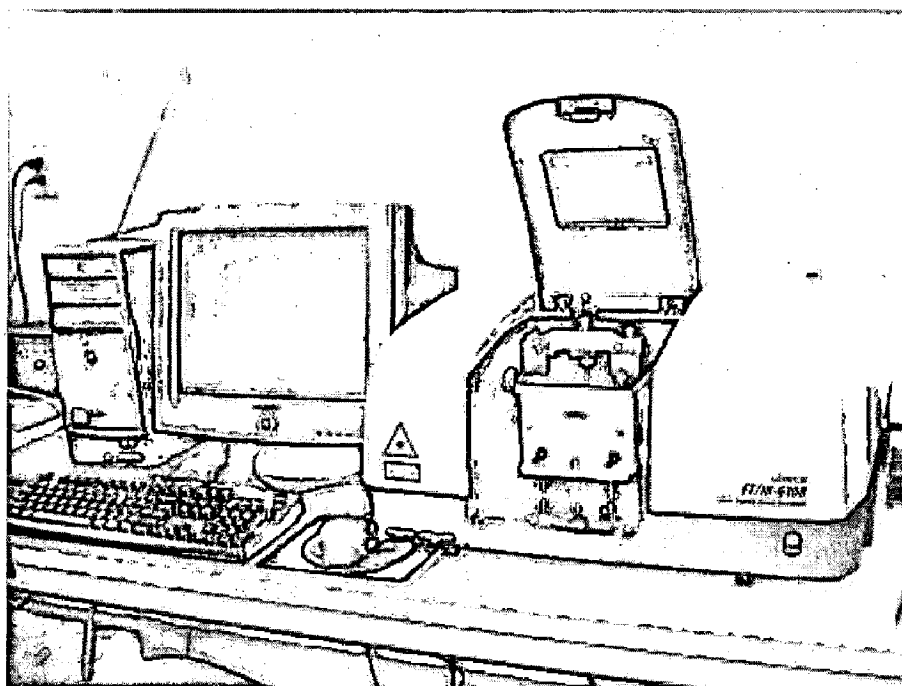

Fig 3 (e) FTIR Spectrophotometer

Infrared light is guided through an interferometer and then through the sample (or vice versa). A moving mirror inside the apparatus alters the distribution of infrared light that passes through the interferometer. The signal directly recorded, called an "interferogram", represents light output as a function of mirror position. A data-processing technique called Fourier transform turns this raw data into the desired result (the sample's spectrum): Light output as a function of infrared wavelength (or equivalently, wavenumber). As described above, the sample's spectrum is always compared to a reference.

Qualitative Analysis
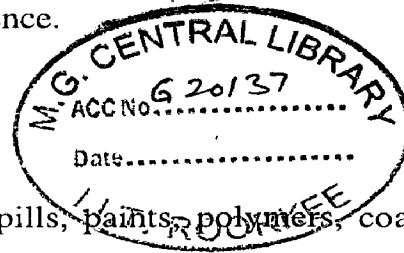
FTIR can be used to identify chemicals from spills, paints, polymers, coatings, drugs, and contaminants. FTIR is perhaps the most powerful tool for identifying types of chemical bonds (functional groups). The wavelength of light absorbed is characteristic of the chemical bond as can be seen in this annotated spectrum.

Quantitative Analysis

Because the strength of the absorption is proportional to the concentration, FTIR can be used for some quantitative analyses. Usually these are rather simple types of tests in the concentration range of a few ppm up to the percent level. For example, EPA test methods 418.1 and 413.2 measure the C-H absorption for either petroleum or total hydrocarbons. The amount of silica trapped on an industrial hygiene filter is determined by FTIR using NIOSH method 7602.

Physical Principles

Molecular bonds vibrate at various frequencies depending on the elements and the type of bonds. For any given bond, there are several specific frequencies at which it can vibrate. According to quantum mechanics, these frequencies correspond to the ground state (lowest frequency) and several excited states (higher

frequencies). One way to cause the frequency of a molecular vibration to increase is to excite the bond by having it absorb light energy. For any given transition between two states the light energy (determined by the wavelength) must exactly equal the difference in the energy between the two states [usually ground state (E_0) and the first excited state (E_1)]. The energy corresponding to these transitions between molecular vibrational states is generally 1-10 kilocalories/mole which corresponds to the infrared portion of the electromagnetic spectrum.

$$\frac{\text{Difference in}}{\text{Energy States}} = \frac{\text{Energy of}}{\text{Light Absorbed}}$$

$$E_1 - E_0 = h\,c\,/\,l$$

Where   h = Planks constant

c = speed of light, and

l = the wavelength of light

Sample Preparation

Samples for FTIR can be prepared in a number of ways. For liquid samples, the easiest is to place one drop of sample between two plates of sodium chloride (salt). Salt is transparent to infrared light. The drop forms a thin film between the plates. Solid samples can be milled with potassium bromide (KBr) to form a very fine powder. This powder is then compressed into a thin pellet which can be analyzed. KBr is also transparent in the IR. Alternatively, solid samples can be dissolved in a solvent such as methylene chloride, and the solution placed onto a single salt plate. The solvent is then evaporated off, leaving a thin film of the original material on the plate. This is called a cast film, and is frequently used for polymer identification.

Solutions can also be analyzed in a liquid cell. This is a small container made from NaCl (or other IR-transparent material) which can be filled with liquid, such

21

as the extract for EPA 418.1 analysis. This creates a longer path length for the sample, which leads to increased sensitivity. Sampling methods include making a mull of a powder with hydrocarbon oil (Nujol) or pyrolyzing insoluble polymers and using the distilled pyrolyzate to cast a film. Materials can be placed in an Attenuated Total Reflectance (ATR) cell and gases in gas cells.

Instrumentation

Fourier Transform Infrared (FTIR) spectroscopy is a novel infrared technique. As a conventional infrared spectroscopy, FTIR is used to detect vibrational transitions of a molecule. The advantage of FTIR compared to conventional infrared spectroscopy is that all wavenumbers are measured at once with help of Michelson interferometer. The incoming light beam to the interferometer is dividing into two beams by beamsplitter, one of which is reflecting from fixed mirror and the second one – from moving mirror. Then, both beams are collected by beamsplitter that passes the resulting beam to the sample compartment with protein film. The interference picture is then automatically calculating into infrared spectrum.

3.3.5. TG/DTA:

Thermal analysis are the techniques in which a physical property of a substance is measured as a function of temperature whilst the substance is subjected to a controlled temperature programme.

Thermogravimetry (TG) is a technique in which the mass of a substance is measured as a function of temperature, while the substance is subjected to a controlled temperature programme. The record is the *thermogravimetric or TG curve*; the mass should be plotted on the ordinate decreasing downwards and temperature (T) or time (t) on the abscissa increasing from left to right.

Differential Thermal Analysis (DTA) is a technique in which the temperature difference between a substance and a reference material is measured as a function of temperature whilst the substance and reference material are subjected to the same controlled temperature programme. The record is the *differential thermal or DTA curve*; the temperature difference (δT) should be plotted on the ordinate with endothermic reactions downwards and temperature or time on the abscissa increasing from left to right.
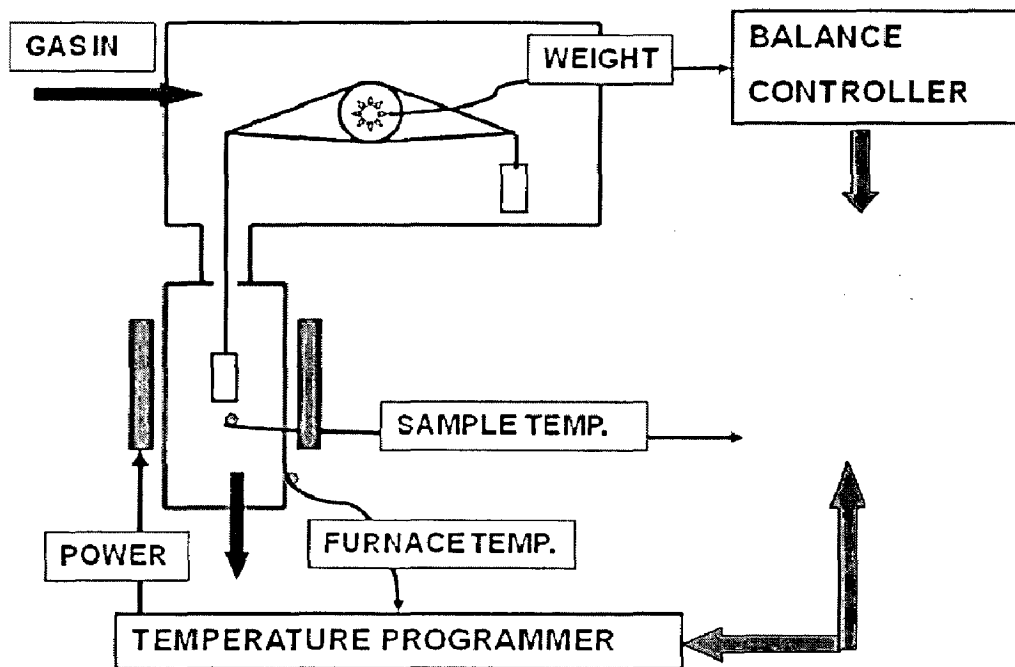

Fig 3 (f) TG working principle

CHAPTER 4

EXPERIMENTAL PROCEDURE

4.1. Sample preparation

0.5M $Ca(NO_3)_2.4H_2O$ (Merck) in ethanol with a pH 10.5 was added to 0.5M $(NH_4)_3PO_4$ (Merck) slowly at a rate of 5 ml/min. and constant temperature (85 °C) with vigorous stirring. The resultant sol–gel was continuously stirred at a constant pH of 10 (pH was kept constant by adding $Ca(OH)_2$ solution) and at a constant temperature of 85 °C for 4 h.


```
                          ┌─────────────────────────┐
                          │  Ca(NO₃)₂.4H₂O +         │
                          │  Ethanol (pH=10.5)       │
                          └─────────────────────────┘
┌──────────────────────┐                │
│ (NH₄)₃PO₄ + Ethanol  │   Vigorous Stirring and
│ (pH= 10.5)           │──▶      Heating
└──────────────────────┘                │
                          ┌─────────────────────────┐
                          │  Sol-Gel (pH=10.5)       │
                          │  Heating at 85 °C        │
                          └─────────────────────────┘
                                   │ Sintering
                          ┌─────────────────────────┐
                          │  Powder at 400 °C        │
                          │  (2Hrs)                  │
                          └─────────────────────────┘
                                   │ Sintering
                          ┌─────────────────────────┐
                          │  Powder at 750 °C        │
                          │  (2Hrs)                  │
                          └─────────────────────────┘
                                   │ Sintering
                          ┌─────────────────────────┐
                          │  Powder at 1200 °C       │
                          │  (2Hrs)                  │
                          └─────────────────────────┘
```
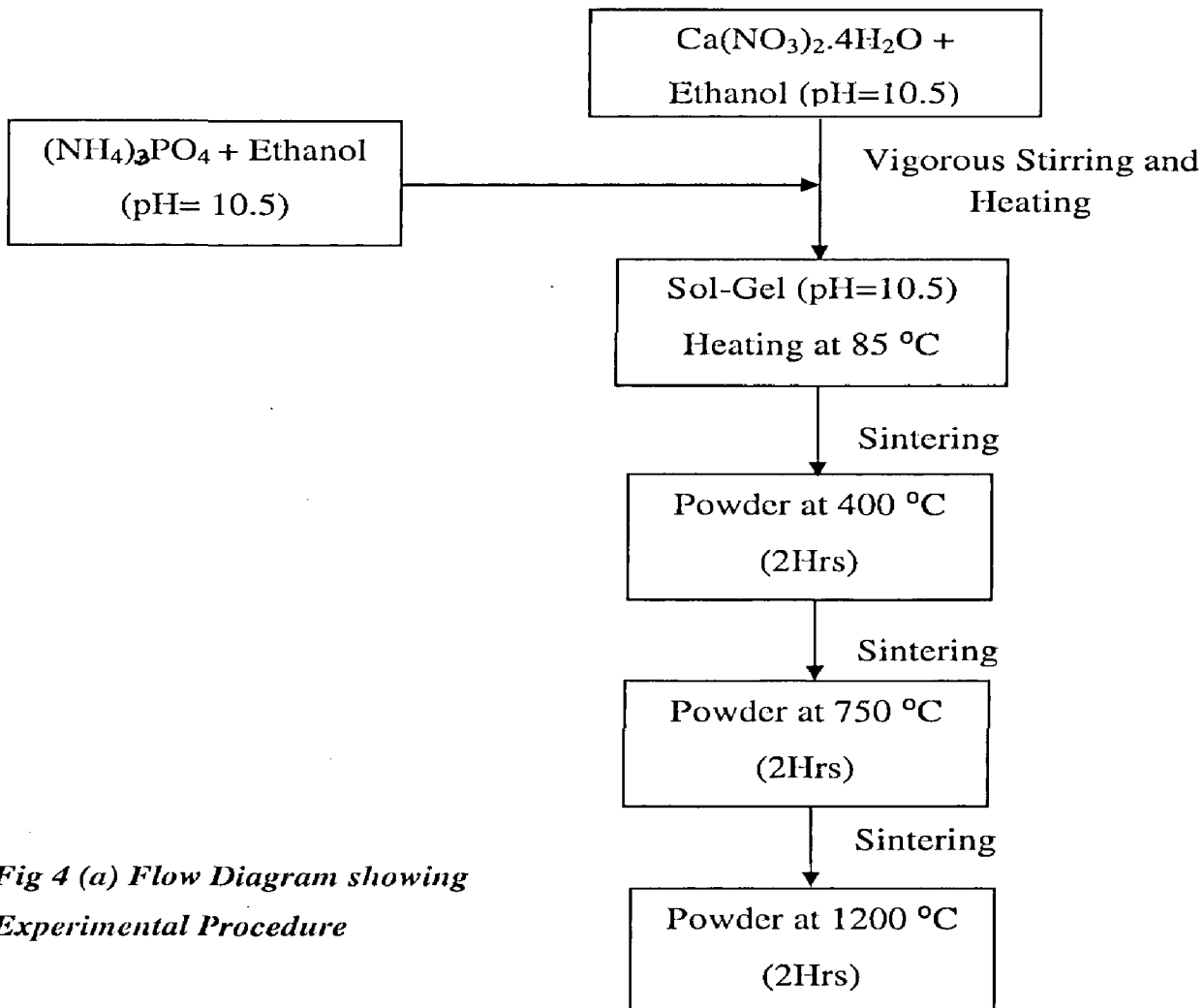
Fig 4 (a) Flow Diagram showing Experimental Procedure

After allowing the product to cool, it was kept inside the oven at 40 °C overnight. The product was sintered for 2 h at 400 °C, again at 750 °C and 1200 °C. The experimental procedure was as shown in the flow diagram given below.

4.2. Characterization of Materials

4.2.1. FT-IR Characterization

A Nicolet 60 SX mid-IR spectrometer, **Nicolet Instruments Corporation, Madison, WI** was used for obtaining the mid-IR FT-IR spectra of the samples in the range of 400–4000 cm^{-1}.All samples were examined in the transmission mode. Samples were mounted in the form of KBr pellets made by thoroughly mixing 1 mg sample powder with 300 mg KBr and pressing in a vacuum die at 1200 p.s.i. (10^3 p.s.i. = 6.89 Nmm^{-2}). The instrument possessed a spectral resolution of 4cm^{-1}.

4.2.2. X-ray Diffraction Characterization

The formation and quality of HAP powders were checked by X-ray diffraction (XRD) technique at room temperature using an X-ray powder diffractometer, **Brucker D8 Advance.**

X-ray diffractograms of samples were taken with Cu Kα radiation (λ = 0.15418 nm) over a wide range of Bragg angles (20° -60 °) with scanning speed 2°/min operated at 30 KV and 30 mA. Samples for XRD characterization were prepared by mounting finely crushed grains on a zero-background holder.

4.2.3. Thermo Gravimetric Analysis

The Thermo gravimetric analysis (TGA) coupled with differential thermal analysis (DTA) of the material was performed between 35 °C and 1000 °C in a **METTLER TA 4000 System** in Nitrogen atmosphere at a heating rate of 10 °C per minute.

4.2.4. Microstructure Analysis

The microstructure and the composition analysis were investigated using an energy dispersive x-ray spectrometer ((EDX) also known as EDS) attached to the field emission scanning electron microscope (FESEM), **FEI, Quanta 200**. The composition analysis was carried out at different spots on the samples by applying accelerating potentials of 20 kV and 15 kV.

CHAPTER 5

RESULTS AND DISCUSSION

5.1. X-ray diffraction patterns (XRD)

The XRD patterns of the as-prepared material at 40 °C and its sintered products at 400 °C, 750 °C and 1200 °C is shown in Fig 5 (a–d), respectively. The pattern due to the as prepared material is not with much resolution and intensity but bear with it the characteristic patterns of HAP. It contains no other crystalline phase other than HAP. The broad patterns around at (002) and (211) indicate that the crystallites are very tiny in nature with much atomic oscillations [43]. Existence of such crystallites was also noticed by van der Houwen et al. [44] during the organic ligands assisted growth of calcium phosphate. Here the mother liquor is expected to permit selective growth of multitudes of HAP crystallites with high rate thus avoiding orderly growth of large crystals.

The XRD patterns of the sintered material at 400 °C (Fig 5 (b)) show increase in intensity due to planes around (002), (210), (211), (310), (222), (213) and (411). Again there is no formation of any new crystalline phase other than HAP. As the patterns appear still broad, the crystals are expected to be still tiny, but bigger than the parent crystallites. Here also there must be significant atomic oscillations. As the growth of many planes is evident, there must be orderly transport of mass to the central growing crystal from the neighbouring ones. In order to verify this, heat-assisted mass transport sintering was also done at 750 °C and 1200 °C (Fig 5 (c-d)). In correspondence with the view, there is gradual increase in the intensity with enhanced resolution was observed for all the diffraction patterns obtained.

Again at the sintering temperature of 1200 °C, new crystalline phases are not seen. This precludes even amorphous phases, as the patterns appear very well resolved. As the increase in intensity is noticed for every pattern with increase in sintering temperature, the growth of crystal need not be due to particle coalescence at the planes of maximum

density. Some studies on HAP has reported transformation of HAP into calcium pyrophosphate at 1200 °C [45]. It was suggested to be due to CaO. The decomposition of HAP partly into tricalcium phosphate was also reported by Raynaud et al. [46].
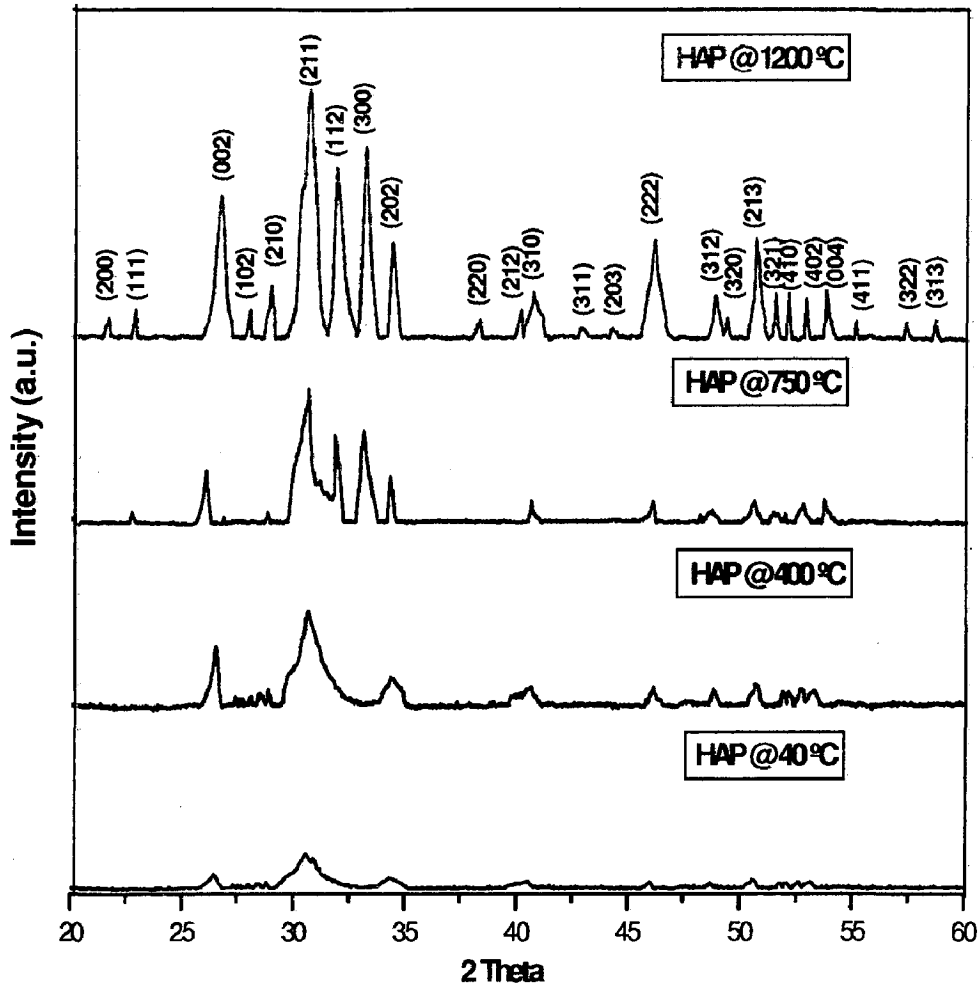

Fig 5(a) XRD patterns: As prepared sample at 40 °C, Sintered at 400 °C, Sintered at 750 °C, Sintered at 1200 °C.

This decomposition into tricalcium phosphate was also not observed in the present study when the material was sintered at 750 °C. Zhou et al. reported transformation of HAP into oxyapatite between 1200 °C and 1400 °C [47], but at 1200 °C no such transformation is observed in the present study.

The average linear particle size (P) of HAP sintered at different temperatures was calculated from strong and medium intensity peaks using

$$\text{Scherrer's equation, } P = (0.9\lambda)/\beta_{1/2}\cos\theta,$$

where $\beta_{1/2}$ is Full width at half maximum intensity.

The particle sizes calculated from above formula are as follows:

(a) HAP as prepared sample = 52nm

(b) HAP sintered at 400 °C = 61nm

(c) HAP sintered at 750 °C = 66nm

(d) HAP sintered at 1200 °C = 73nm

It is evident that the crystal growth contributes to the increase in reflection intensity, as depicted in Fig. 5 (a). The particle size increases from 61nm at 400°C to 73nm at 1200°C.

5.2. Fourier Transform Infrared (FTIR) Spectroscopy

The FTIR spectra of the samples were obtained in the range 400 cm^{-1} – 4000 cm^{-1} and following results were obtained:

5.2.1. Raw Sample:

The FTIR spectrum of the as prepared material is shown in Fig 5(b). The spectrum shows a broad envelope between 3800 and 2800 cm^{-1} due to the O–H stretch of water and HAP. The O–H groups are hydrogen bonded. The sharp edge at 3566 cm^{-1} is assigned to unhydrogen bonded free O–H stretch which may be present at the surface of the crystallites. The peak at 1636 cm^{-1} is assigned to bending mode of water. The absorption band at 1400 cm^{-1} is attributed to the presence of carbonate and/or hydrogen phosphate in the sample [31, 41]. The intense peaks between 950 and 1190 cm^{-1} is assigned to PO_4^{-3}. The stretching and the bending modes of PO_4^{-3} appeared at 1148, 1080, 1030, 940, 720 and 570 cm^{-1} as intense sharp peaks.

Van der Houwen et al. reported identification of HPO_4^{-2} based on its water absorption bands at 1210 cm^{-1} together with one at 1130 cm^{-1} (shoulder to the absorption band at 1099 cm^{-1}) and a clear absorption band at 879 cm^{-1}. But these features are not clearly evident in the spectrum, as the absorption band due to PO_4^{-3} of HAP is intense and broad. But the distinct peak at 868cm^{-1} indicates the presence of HPO_4^{-2} in the

structures. They also reported dissolving of atmospheric CO_2 yielding CO_3^{-2} based on the peaks at 1456 cm^{-1} and 873 cm^{-1} as the crystallization was carried out in alkaline range (pH=10.5) [32].
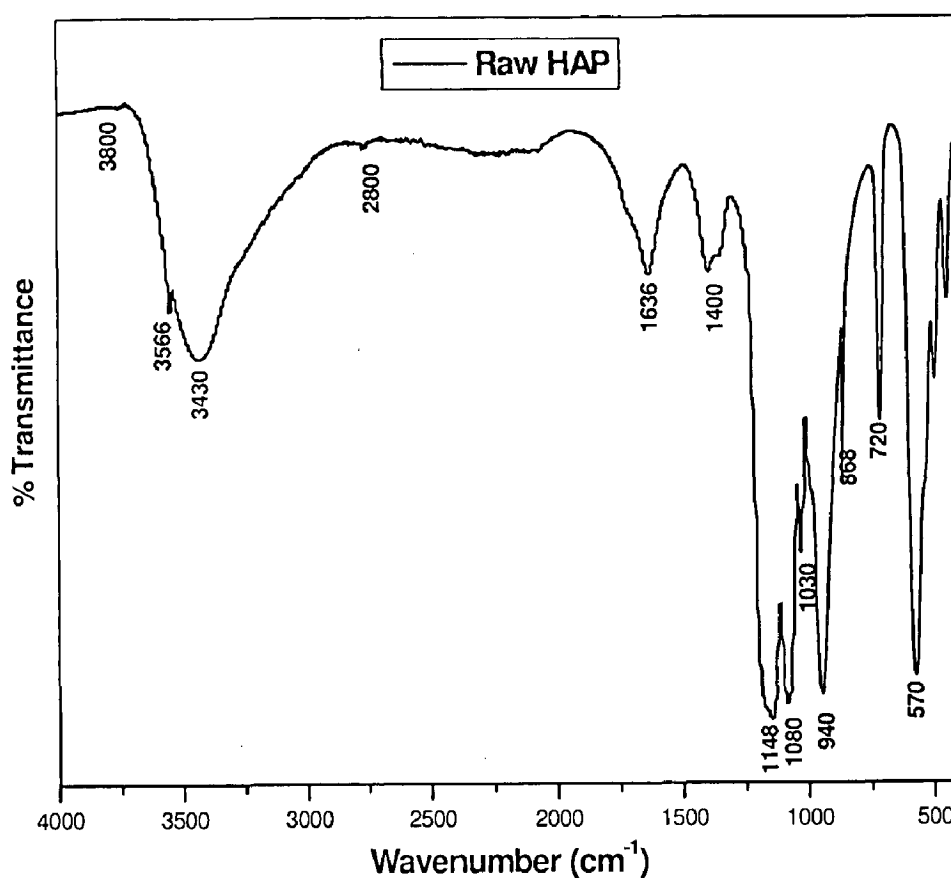

Fig 5(b) FTIR Spectra of as prepared sample

Since the present experiment was also done in the alkaline range similar process should also occur. But in the IR spectrum, there is no sharp peak at 1456 and 873 cm^{-1} in the spectrum of the as-prepared material. But this peak is somewhat more evident in the spectra of sintered materials. The peaks at 3566 cm^{-1} and 624 cm^{-1} are the characteristic peaks of HAP, and it can be seen in the figure, confirming the presence of stoichiometric HAP.
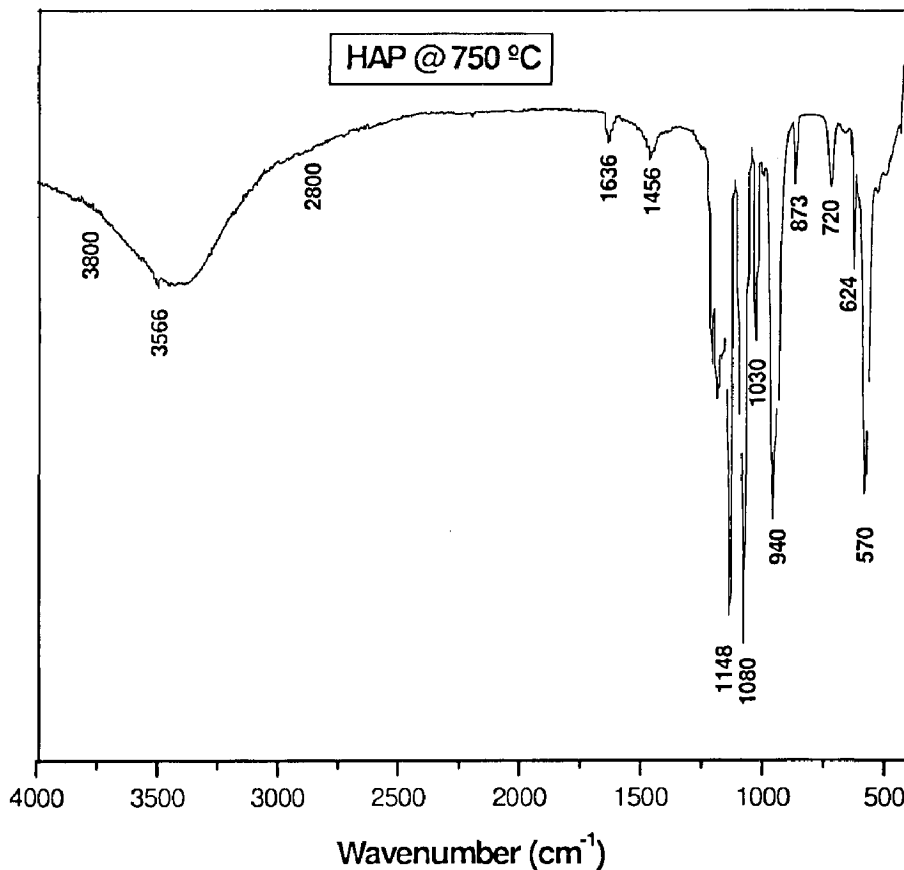
5.2.2. Sample sintered at 400 °C:

The FTIR spectrum of the material sintered at 400 °C is shown in Fig 5(c). It also shows a broad envelope between 3800 cm^{-1} and 2800 cm^{-1} due to the O–H stretch of water and HAP and show peak at 1636 cm^{-1} due to bending mode of water. The sharp edge at 3566 cm^{-1} is assigned to unhydrogen bonded free O–H stretch which may be present at the surface of the crystallites. The absorption band at 1400 cm^{-1} is due to the presence of carbonate and/or hydrogen phosphate in the sample [31, 41].
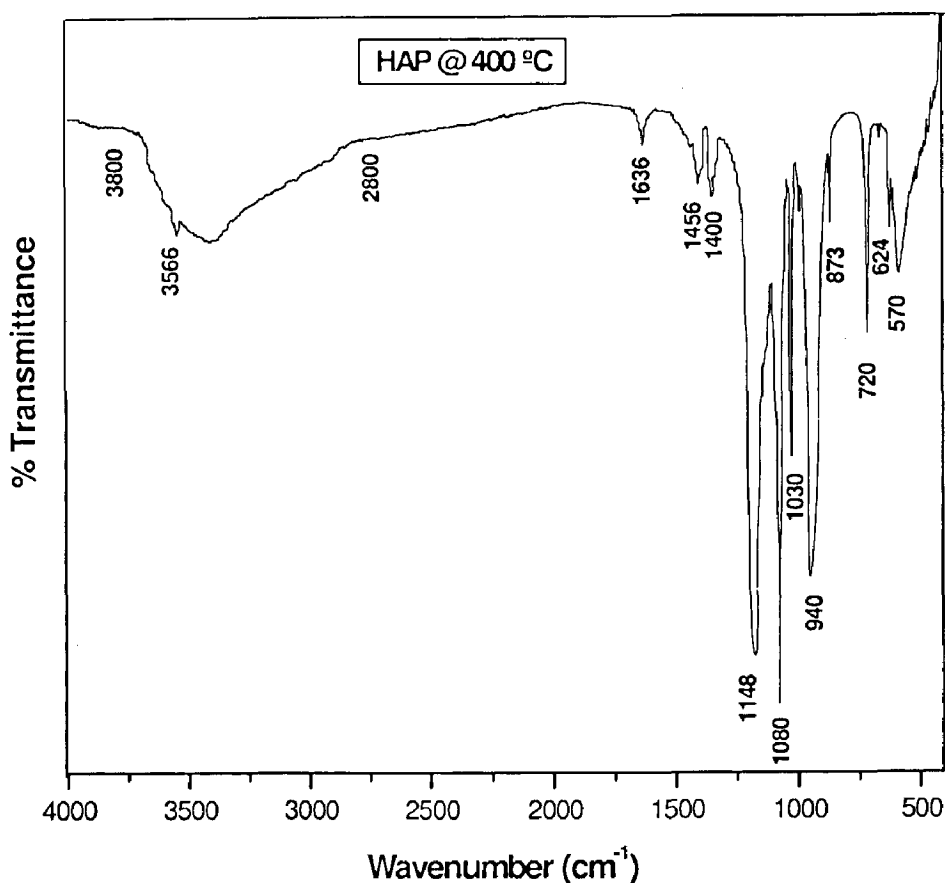
Fig 5 (c) FTIR Spectra of the sample at 400 °C

The intense peaks between 950 and 1190 cm^{-1} is assigned to PO $^{-3}$. The stretching and the bending modes of PO_4 $^{-3}$ appeared at 1148, 1080, 940, 720 and 570 cm^{-1} as intense sharp peaks. The peaks at 1456 cm^{-1} and 873 cm^{-1} confirms the dissolving of atmospheric CO_2 yielding CO_3^{-2} as the crystallization was carried out in alkaline range

(pH=10.5) [32]. Elliot et al. reported absorption of non-structural carbonate at the surface of HA at 1456, 1412 and 873cm^{-1}[34, 42]. In the IR spectra of the materials sintered at 400 °C (Fig 5c), the first two peaks are partly evident although the last is common HPO_4^{-2} vibrations. The peaks at 3566 cm^{-1} and 624 cm^{-1} are the characteristic peaks of HAP, and it can be seen in the figure, confirming the presence of stoichiometric HAP.
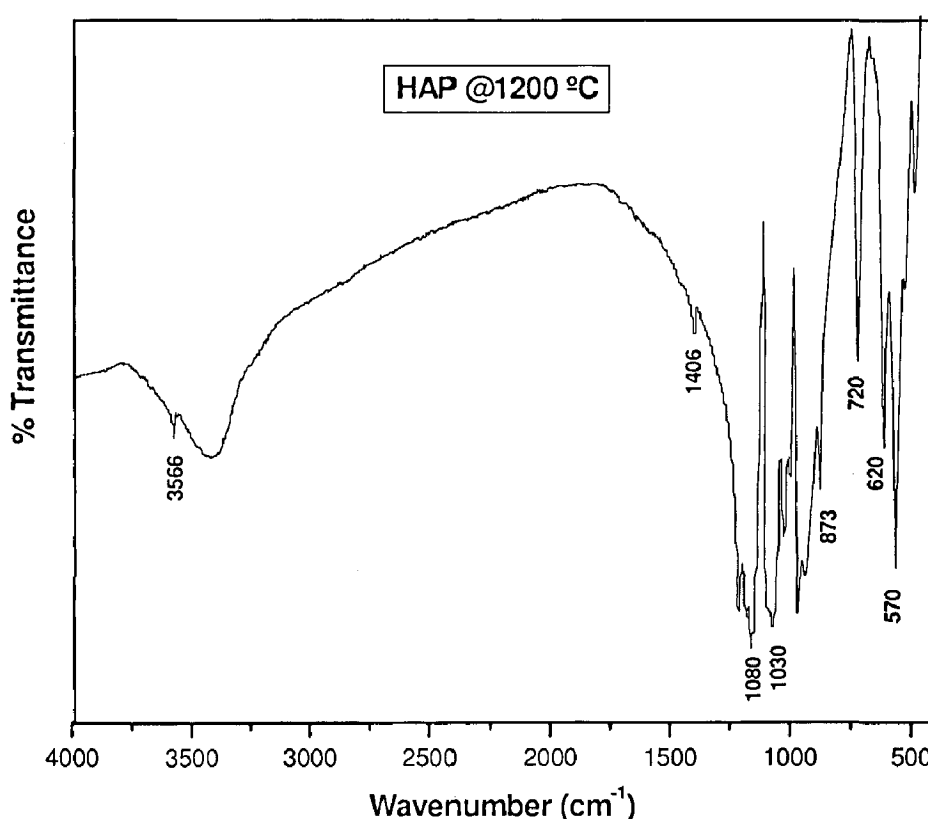
5.2.3. Sample sintered at 750 °C:

Fig 5(d) FTIR Spectra of the sample at 750 °C

The FTIR spectrum of the material sintered at 750 °C is shown in Fig 5(d). It also shows a broad envelope between 3800 cm^{-1} and 2800 cm^{-1} due to the O–H stretch of water and HAP. The peak at 1636 cm^{-1} is assigned to bending mode of water. The absorption band at 1400 cm^{-1} is attributed to the presence of carbonate and/or hydrogen phosphate in the sample [31, 42]. The intense peaks between 950 and 1190 cm^{-1} is

assigned to PO_4^{-3}. The stretching and the bending modes of PO_4^{-3} appeared at 1148, 1080, 1030, 940, 720 and 570 cm^{-1} as intense sharp peaks. The peaks at 1456 cm^{-1} and 873 cm^{-1} also appeared due to dissolving of atmospheric CO_2 yielding CO_3^{-2} as the crystallization was carried out in alkaline range (pH=10.5) [32]. The peaks at 1456, 1412 and 873cm^{-1} confirms non-structural carbonate at the surface of HAP [34, 41]. The peaks at 3566 cm^{-1} and 624 cm^{-1} are the characteristic peaks of HAP, and it can be seen in the figure, confirming the presence of stoichiometric HAP.

5.2.4. Sample sintered at 1200 °C:


Fig 5(e) FTIR Spectra of the sample at 1200 °C

The FTIR spectrum of the material sintered at 1200 °C is shown in Fig 5(e). It also shows a broad envelope between 3800 and 2800 cm^{-1} due to the O–H stretch of water and HAP. The absorption band at 1400 cm^{-1} is attributed to the presence of carbonate and/or hydrogen phosphate in the sample [31, 42]. The intense peaks between

950 and 1190 cm^{-1} is assigned to PO_4^{-3}. The stretching and the bending modes of PO_4^{-3} appeared at 1080, 1030, 940, 720 and 570 cm^{-1} as intense sharp peaks.

The peaks at 1456 and 873 also appeared due to dissolving of atmospheric CO_2 yielding CO_3^{-2} as the crystallization was carried out in alkaline range (pH=10.5) [32]. The peaks at 1456, 1412 and 873cm^{-1} confirms non-structural carbonate at the surface of HAP [34, 41]. The peaks at 3566 cm^{-1} and 624 cm^{-1} are the characteristic peaks of HAP, and it can be seen in the figure, confirming the presence of stoichiometric HAP.

5.3. Thermogravimetric analysis
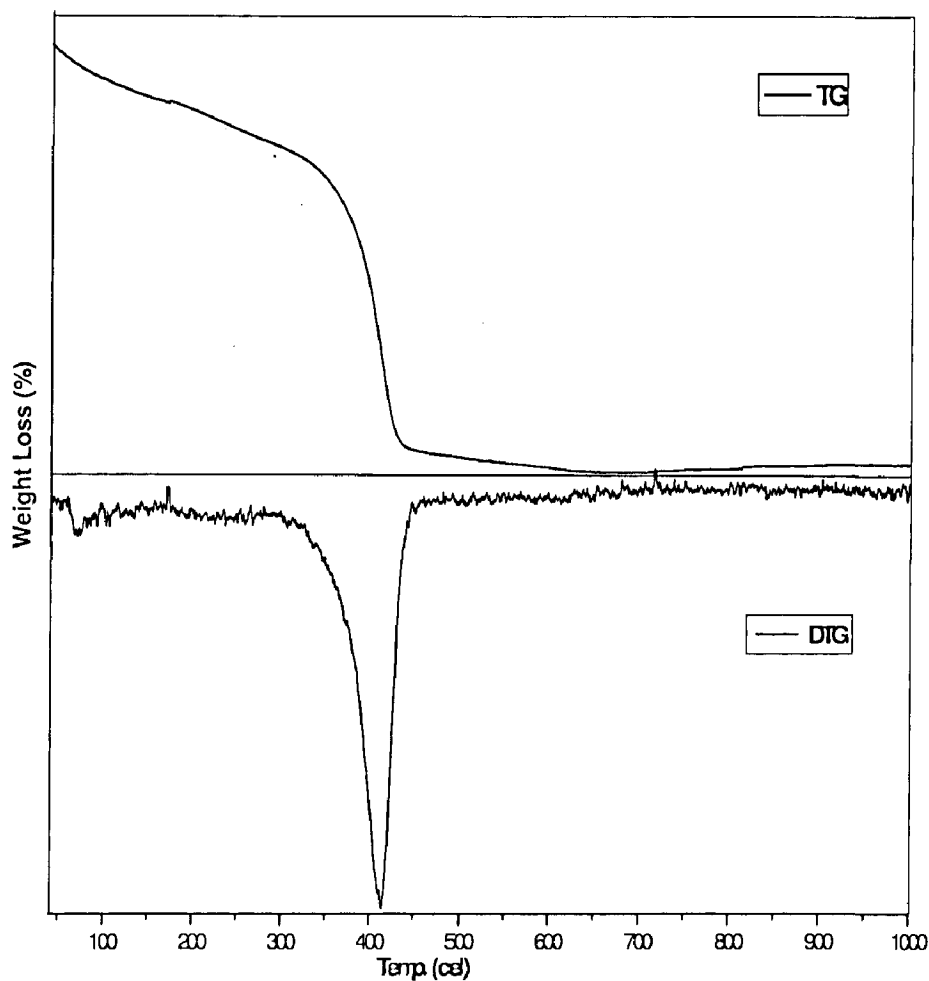
Fig. 5 (f) TGA/DTG of as prepared sample

The thermogravimetric analysis of the as prepared sample was carried out between 35 °C and 1000 °C in Nitrogen atmosphere at a heating rate of 10 °C /min using Alumina as the reference. The thermogram and its differential thermogravimetric trace are shown in Fig 5 (f). There is a minute weight loss (1.1%) around 300 °C. It is assigned to weakly entrapped water in the material.

It is followed by major weight loss (2.6%) between 300 °C and 450 °C. It is assigned to the dehydration of calcium hydroxide [29]. The decomposition trace does not bear any inflection, and this process is also not accompanied by any other additional decomposition. Hence there might be only one phase involved in the decomposition. There is a minute weight loss (0.2%) between 450 °C and 650 °C. It is assigned to decomposition of calcium hydroxide and carbonate to water and carbon dioxide [30].

5.4. Scanning electron microscopy (SEM)

The SEM picture of as prepared sample is shown in Fig 5(g). The sintered material at 400°C and 750 °C is shown in Fig 5(h), 5(i).
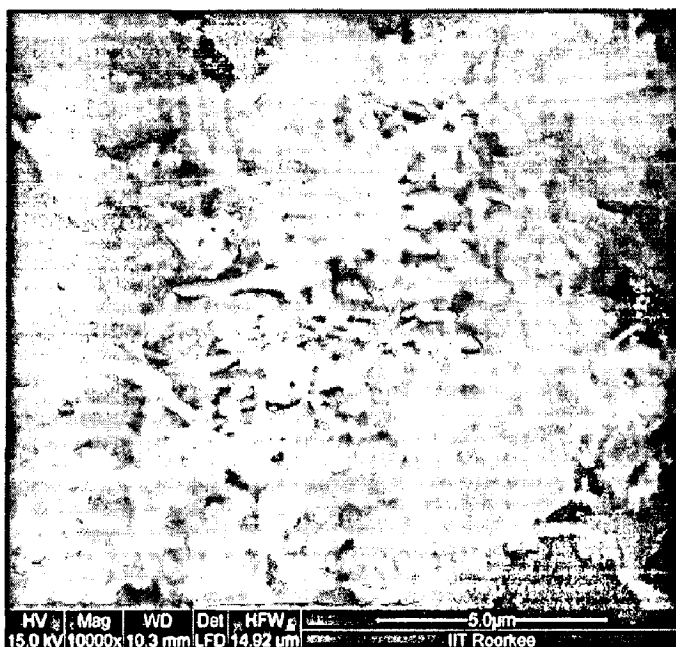

Fig 5(g) Scanning electron micrograph of the as prepared sample

The as prepared sample shows the presence of flakes of HAP, which on sintering at higher temperature forms rod-shaped agglomerates and crystallites of nanometer size

35

with a tendency to agglomerate leaving pores in between. To test this, the material was sintered at 1200°C and subjected to SEM analysis. The SEM picture is shown in Fig 5(j).
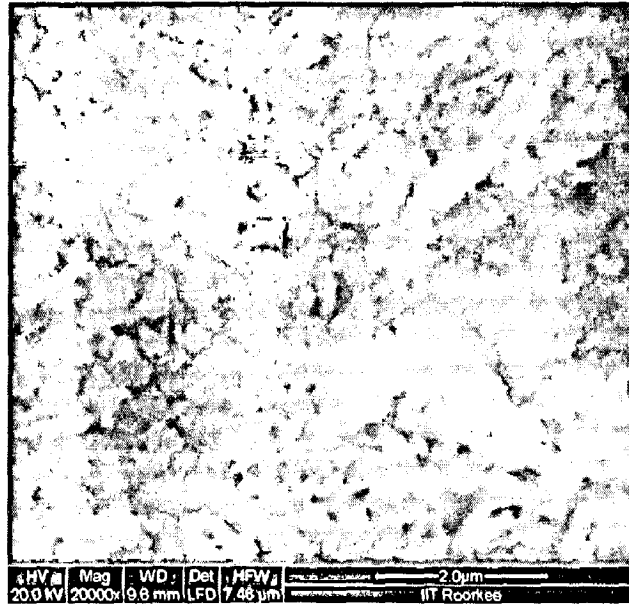

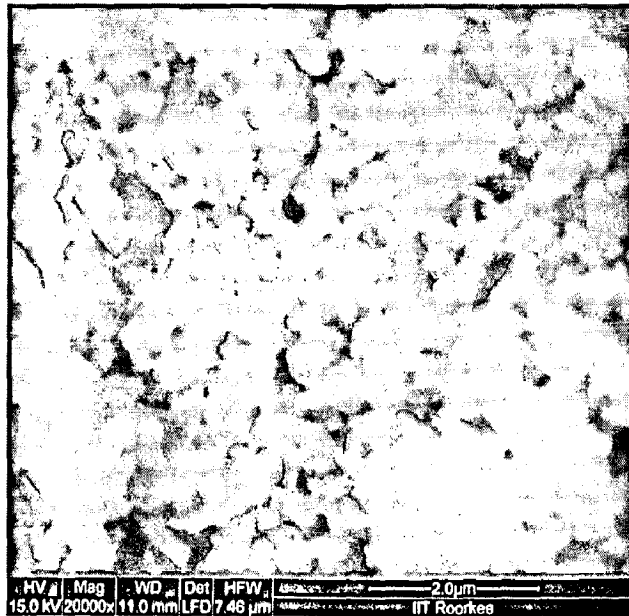*Fig 5(h) Scanning electron micrograph of the sample at 400 °C*

Fig. 5(i) Scanning electron micrograph of the sample at 750 °C

There are dense agglomerates with distributed pores in them. The formation of pores is beneficial, as they would permit the circulation of the physiological fluid throughout the coatings when it is used as biomaterial.
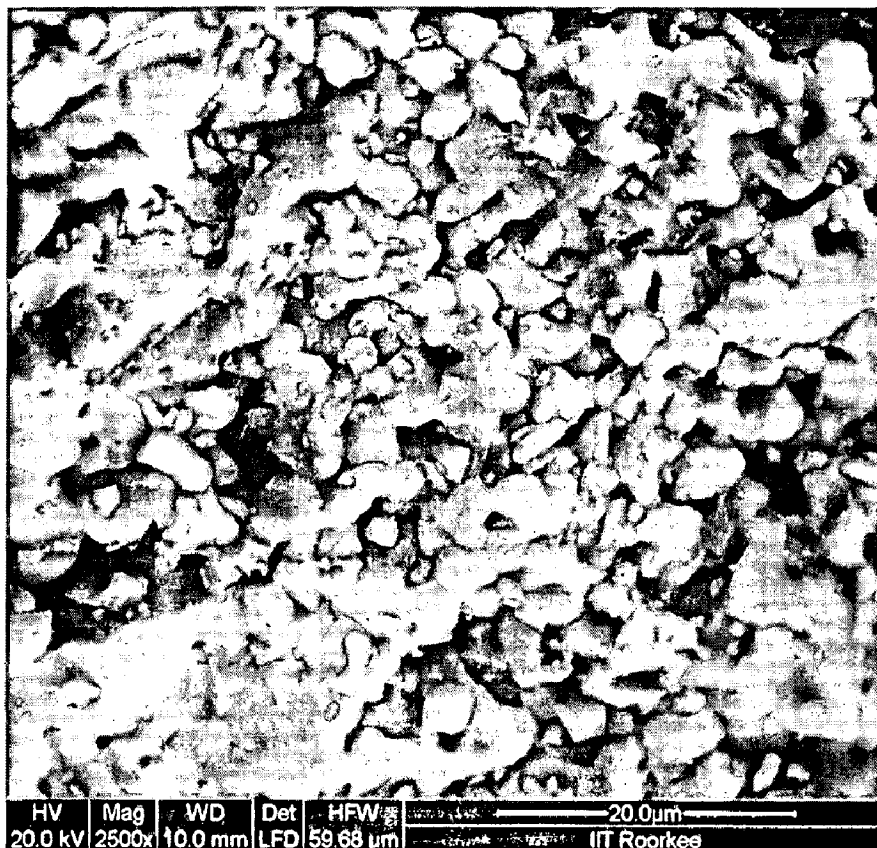

Fig. 5(j) Scanning electron micrograph of the sample at 1200 °C

5.5. EDAX ANALYSIS:

The composition analysis of the HAP samples determined by the EDAX analysis is shown in figure 5 (k)-(n).
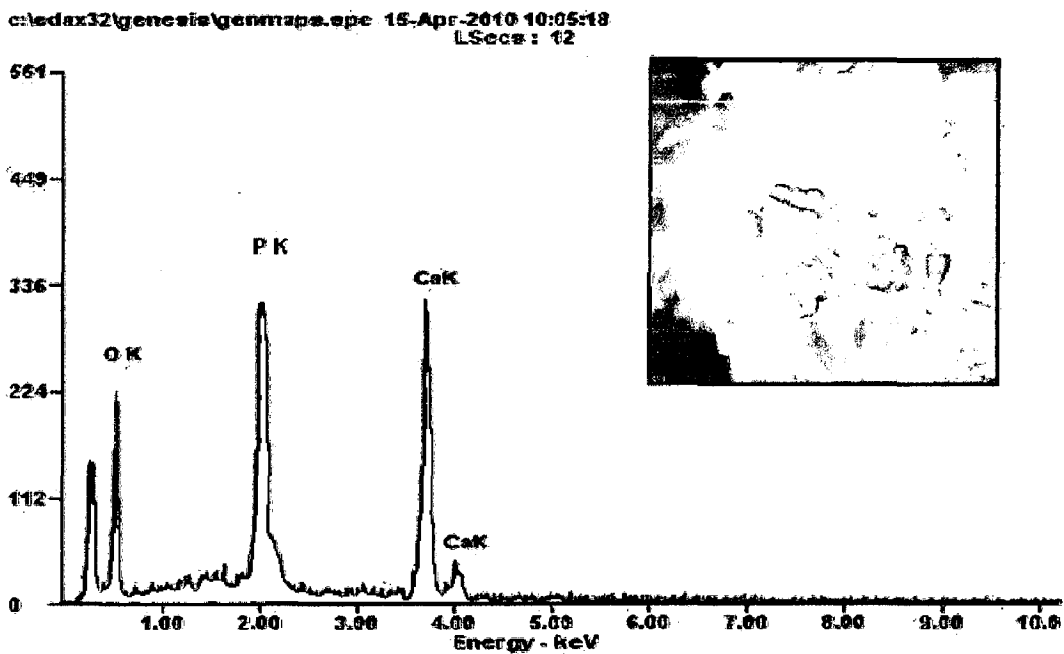

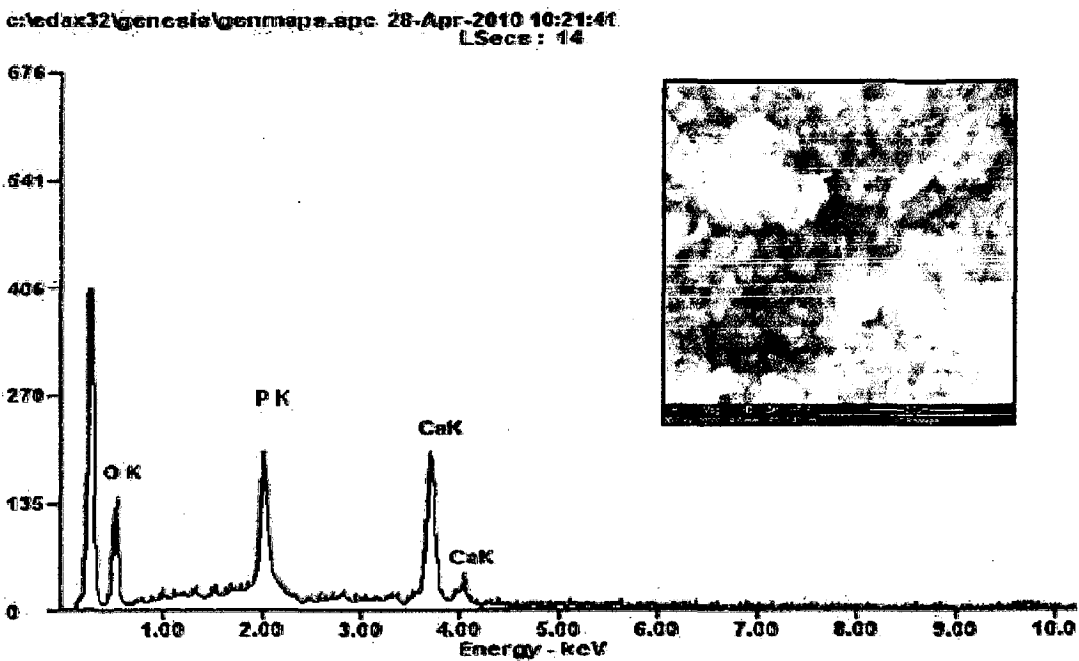*Fig 5 (k) EDAX plot of as prepared sample*

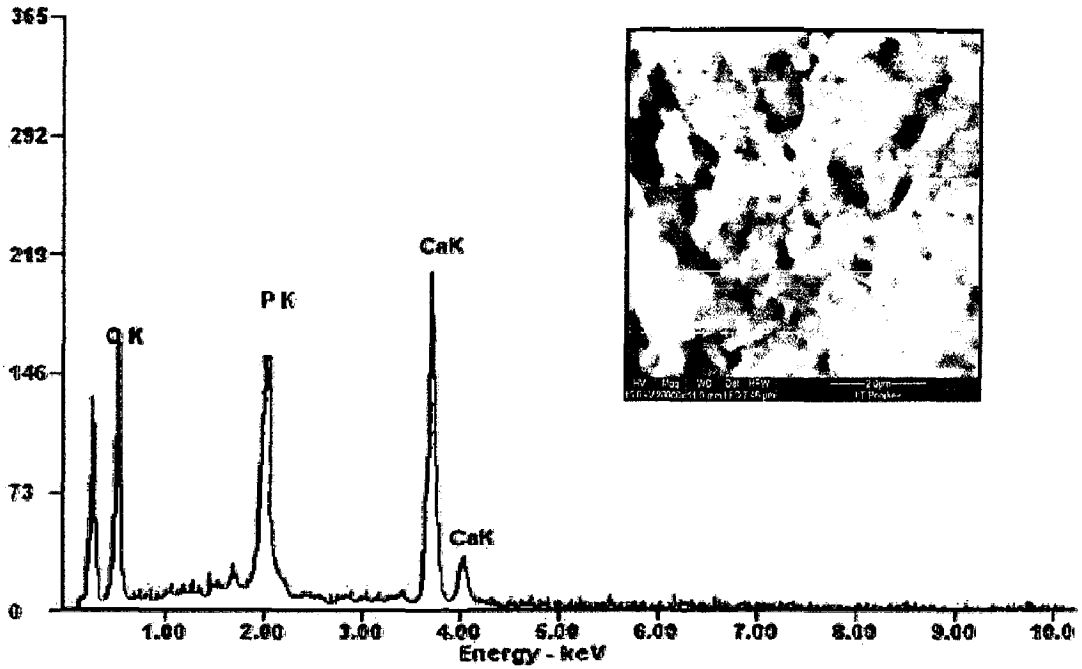*Fig 5 (l) EDAX plot of sample sintered at 400 °C*

38

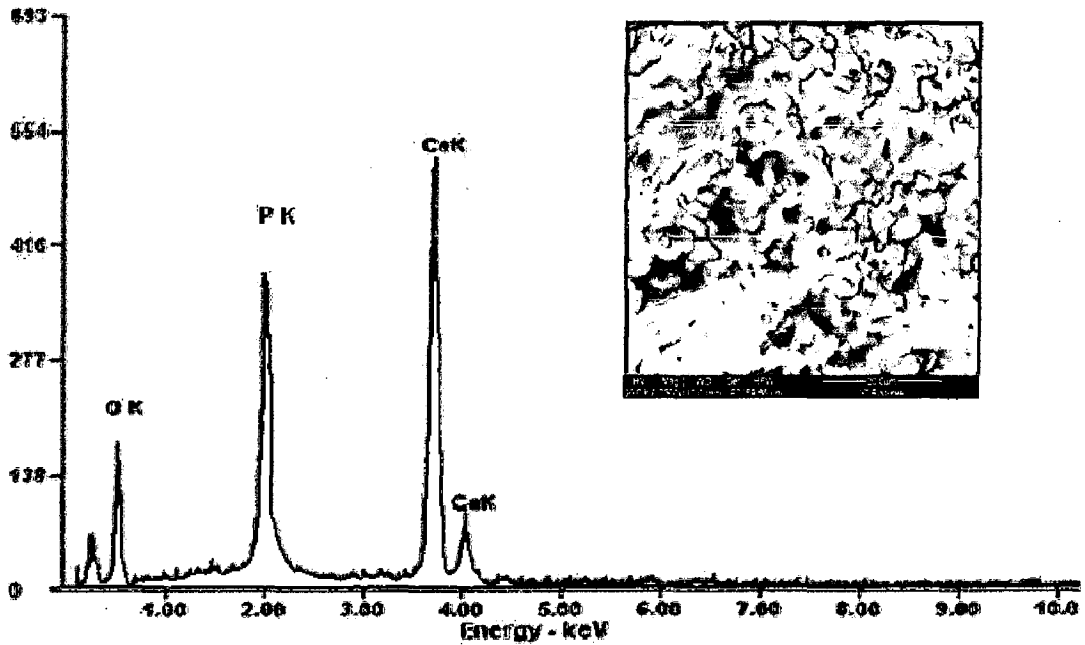*Fig 5 (l) EDAX plot of sample sintered at 750 °C*

Fig 5 (l) EDAX plot of sample sintered at 1200 °C

In the EDAX analysis it can be seen that all of the HAP samples have a Ca:P ratio of approximately 1.67, which is same as is present in human bone.

CONCLUSION

In this Dissertation report, a relatively easy method to synthesize pure, stable, stoichiometric nanocrystalline Hydroxyapatite i.e. $Ca_{10}(PO_4)_6(OH)_2$ (HAP) at low temperature at alkaline pH via an ethanol based sol–gel route was presented using equimolar solutions of $Ca(NO_3)_2.4H_2O$ and $(NH_4)_2HPO_4$ dissolved in ethanol at 85 °C and the product so formed was sintered at three different temperatures, i.e. 400 °C, 750 °C and 1200 °C. These sintered samples along with the as prepared sample were then characterized by X-Ray Diffraction (XRD), Fourier Transform IR spectroscopy (FTIR), Scanning Electron Microscopy (SEM), Energy Dispersive X-ray spectroscopy (EDAX) and Thermogravimetric analysis (TGA)/Differential Thermal Analysis (DTA) for checking the formation and quality of desired product, for checking its stability at higher temperatures and for microstructural and compositional analysis.

The ethanol-based synthesis seems to provide a thermally stable hydroxyapatite even at high temperature of 1200 °C.

This method of synthesis also produced nanocrystalline HAP in the range of 50 - 80 nm in diameter, which would make them ideal bone replacement material. The presence of pores in the crystal planes itself will help the material to attain more biocompatibility and will enable the circulation of physiological fluids.

By this process, we can prepare pure, stoichiometric, nanocrystalline HAP, needed for various biomaterial applications.

REFERENCES

1. Dean-Mo Liu and Quanzu Yang, "Structural evolution of sol–gel-derived hydroxyapatite", Biomaterials 23 (2002) 1679–1687.

2. Posner AS. "Crystal chemistry of bone mineral". Physiol Rev 1969;49(4):760–92.

3. BerryEE. "The structure and composition of some calcium deficient apatite". J Inorg Nucl Chem 1967; 29:317–27.

4. Eastoe JE. "The chemical composition of bone". In: Long C, editor. Biochemists handbook. Princeton, NJ: Van Nostrand, 1961. p. 715–20.

5. Glimcher MJ. "Recent studies of the mineral phase in bone and its possible linkage to the organic matrix byprotein-bound phosphate bonds". Trans R Soc London 1984; 304B: 479–508.

6. Jarcho M. "Calcium phosphate ceramics as hard tissue prosthetics". Clin Orthop 1981; 157:259–78.

7. Ducheyne P, Hench LL, Kagan A, Martens M, Bursens A, Mulier JC. "Effect of hydroxyapatite impregnation on skeletal bonding of porous coated implants". J Biomed Mater Res 1980; 14:225.

8. Hench LL. Bioceramics: from concept to clinic. J Am Ceram Soc 1991; 74:1487–510.

9. Ducheyne P, Cuckler JM. "Bioactive ceramic prosthetic coatings". Clin Orthop Relat Res 1992; 276:102–14.

10. Masuda Y, Matubara K, Sakka S. "Synthesis of hydroxyapatite from metal alkoxides through sol–gel technique". J Ceram Soc Japan 1990; 98:1266–77.

11. Brendel T, Engel A, Russel C. "Hydroxyapatite coatings by a polymeric route". J Mater Sci Mater Med 1992; 3:175–9.

12. Gross KA, Chai CS, Kannangara GSK, Bin-Nissan B, HanleyL. "Thin hydroxyapatite coatings via sol–gel synthesis". J Mater Sci Mater Med 1998; 9:839–43.

13. Hwang K, Lim Y. "Chemical and structural changes of hydroxyapatite films by using a sol–gel method". Surf Coating Tech 1999; 115:172–5.

14. Haddow DB, James PF, Van Noort R. "Characterization of sol–gel surfaces for biomedical applications". J Mater Sci Mater Med 1996; 7:255–60.

15. Lopatin CM, Pizziconi V, Alford TL, Laursen T. "Hydroxyapatite powders and thin films prepared bya sol–gel technique". Thin Solid Films 1998; 326:227–32.

16. Liu DM, Troczynski T, Tseng WJ. "Water-based sol–gel synthesis of hydroxyapatite: process development". Biomaterials 2001; 22:1721–30.

17. Hwang K, Song J, Kang B, Park Y. "Sol–gel derived hydroxyapatite films on alumina substrates". Surf Coat Tech 2000; 123:252–5.

18. Layrolle P, Ito A, Takishi T. "Sol–gel synthesis of amorphous calcium phosphate and sintering into microporous hydroxyapatite bioceramics". J Am Ceram Soc 1998; 81(6):1421–8.

19. Liu DM, Troczynski T, Tseng WJ. "Aging effect on the phase evolution of sol–gel hydroxyapatite". Biomaterials, 2002, 23, 1227-1236.

20. A. JILLAVENKATESA, R. A. CONDRATE SR, "Sol gel processing of hydroxyapatite", Journal of Materials Science 33 (1998) 4111 – 4119.

21. R. Z. Legeros and J. P. Legeros, in "An Introduction to Bioceramics", edited by L. L. Hench and J. Wilson (World Scientific, Singapore 1995) p. 139.

22. E. C. Shors and R. E. Homes, *ibid.*, p. 181.

23. F. J. Callens, R. M. H. Verbeeck, D. Nassens, P. F. A. Matthys and E. R. Boesman, *Calc. issue Int.* 44 (1989) 114.

24. F. J. Callens, R. M. H. Verbeeck, P. F. A. Matthys, L. C. Martens, E. R. Boesman and F. C. M. Driessens, *Bull. Soc. Chim. Belg.* 96 (1987) 165.

25. S. Stea, M. Visentin, L. Savarino, et al., J. Mater. Sci. Mater. Med. 6 (1995) 455–459.

26. S. Overgaard, M. Lind, K. Josephsen, A.B. Maunsbach, C. Bunger, K. Soballe, J. Biomed. Mater. Res 39 (1998) 141–152.

27. K. Hayashi, T. Mashima, K. Uenoyama, Biomaterials 20 (1999) 111–119.

28. L.D. Piveteau, B. Gasser, L. Schlapbach, Biomaterials 21 (2000) 2193–2201.

29. T.K. Anee, M. Ashok, M. Palanichamy, S.N. Kalkura, Mater. Chem. Phys. 80 (2003) 725.

30. D.M. Liu, Q. Yang, T. Trocznski, W.J. Tseng, Biomaterials 23 (2002) 1679.

31. J.A.M. van der Houwen, G. Cressey, B.A. Cressy, E. Valsami-Jones, J. Crystal Growth 249 (2003) 572.

32. S. Raynaud, E. Champion, D. Bernache-Assollant, P. Thomas, Biomaterials 23 (2002) 1065.

33. J. Zhou, J. Chen, X. Zhang, K. De Groot, J. Mater. Sci. Mater. Med. 4 (1993) 83.

34. J.C. Elliot, Structure and Chemistry of the Apatites and Other Calcium Ortho phosphates, Elsevier, Amsterdam, 1994, p.389.

35. W.L. Suchanek, P. Shuk, K. Byrappa, R.E. Riman, K.S. Ten Huisen, V.F. Janes, Biomaterials 23 (2002) 699.

36. APHA, Standard Methods for the Examination of Water and Waste Water, 17th Edition, American Water Works Association, New York, 1989.

37. Wenjian Weng and Sam Zhang, Sol gel preparation of bioactive apatite films, Surface and Coatings Technology 167 (2003) 292–296.

38. C.M. Lopatin and V. Pizziconi, "Hydroxyapatite powders and thin films prepared by a sol-gel technique", Thin Solid Films 326 (1998) 227–232.

39. E. Tkalcec and M. Sauer, "Sol–gel preparation of bioactive apatite films", J. Mater. Sci. 36 (2001) 5253–5263.

40. M.P. Ferraz, F.J. Monteiro, C.M. Manuel, Hydroxyapatite nanoparticles: A review of preparation methodologies, Journal of Applied Biomaterials & Biomechanics 2004; 2: 74-80.

41. I. Rehman and W. Bonfield, "Characterization of hydroxyapatite and carbonated apatite by photo acoustic FTIR spectroscopy", JOURNAL OF MATERIALS SCIENCE: MATERIALS IN MEDICINE 8 (1997) 1-4.

42. J. C. Elliot, D. W. Holcomb and R. A. Young, "Infrared determination of the degree of substitution of hydroxyl by carbonate ions in human dental enamel", Calcified tissue Int. 37 (1985) 372-375.

43. R.C. Reynolds Jr., Diffraction by Small and Disordered Crystals in Reviews in Mineralogy, Vol. 20, Mineralogical society of America, Book Crafters Inc., Michigan, 1989, p. 369.

44. J.A.M. van der Houwen, G. Cressey, B.A. Cressy, E. Valsami-Jones, J. Crystal Growth 249 (2003) 572.

45. T.K. Anee, M. Ashok, M. Palanichamy, S.N. Kalkura, Mater. Chem. Phys. 80 (2003) 725.

46. S. Raynaud, E. Champion, D. Bernache-Assollant, P. Thomas, Biomaterials 23 (2002) 1065.

47. J.A.M. van der Houwen, G. Cressey, B.A. Cressy, E. Valsami-Jones, J. Crystal Growth 249 (2003) 572.

48. Bajpai PK, Fuchs CM, and Strnat MAP. 1985. Development of alumino-calcium phosphorous oxide (ALCAP) ceramic cements. In: *Biomedical Engineering. IV. Recent Developments*. Proceedings of the Fourth Southern Biomedical Engineering Conference, Jackson, MS, B Sauer, Ed., pp. 22–25. Pergamon Press, New York, pp. 22–25.

49. Park JB and Lakes RS. 1992. *Biomaterials—An Introduction,* 2nd ed., Plenum Press, New York.